Climate Dynamics
https://doi.org/10.1007/s00382-023-07069-y

ORIGINAL ARTICLE

# Large diversity in AMOC internal variability across NEMO-based climate models

**Alcide Zhao[1] · Jon Robson[1,2] · Rowan Sutton[1,2] · Michael W.K. Lai[3] · Jennifer V. Mecking[4] · Stephen Yeager[5] · Tillys Petit[1,2]**

Received: 28 July 2023 / Accepted: 15 December 2023


**Abstract**
We characterise, and explore the drivers of, differences in the internal variability of the atlantic meridional overturning circulation (AMOC) across five NEMO-based CMIP6 class climate models. While the variability of AMOC variability is dominated by its lower dense limb in all models, there is large diversity in the timescale, multidecadal variability, and latitudinal coherence of AMOC across models. In particular, the UK models have much weaker AMOC multidecadal variability and latitudinal coherence. The model diversity is associated with differences in salinity-governed surface density variations which drive high-density water mass transformation (WMT) in the Greenland–Iceland–Norwegian Seas (GIN) and the Arctic. Specifically, GIN Seas WMT shows large multidecadal variability which has a major impact on AMOC variability in non-UK models. In contrast, the smaller variability in GIN Seas WMT in the UK models has limited impact on the lower latitude AMOC via the Denmark strait overflow mass transport. This leads to a latitudinally less coherent and weaker multidecadal variability of the AMOC lower limb. Such differences between UK and non-UK models are related to differences in model mean states and densification processes in the Arctic and GIN Seas. Consequently, we recommend further in-depth studies to better understand and constrain processes driving salinity changes in the Arctic and GIN Seas for more reliable representation of the AMOC in climate models.

## 1 Introduction

The Atlantic meridional overturning circulation (AMOC) plays a pivotal role in shaping the mean state and variability of the North Atlantic climate system and beyond (Zhang et al. 2019). Changes to AMOC, therefore, have profound impacts on various aspects of the Earth system (Yeager and Robson 2017; Bellomo et al. 2021; Jackson et al. 2022). Although there are various hypotheses revolving around the drivers and causes of AMOC changes on various timescales, model studies suggest that AMOC is sensitive to changes in external forcing, for example: solar radiation and volcanic emissions (Pausata et al. 2015; Ye et al. 2023), greenhouse gas emissions (Bakker et al. 2016; Hu et al. 2020), and aerosol forcing (Hassan et al. 2020; Menary et al. 2020a). Climate models project that future AMOC is likely to slow down as global warming continues (Weijer et al. 2020; Liu et al. 2020). However, such projections are uncertain due to many factors (Reintges et al. 2017; Bellomo et al. 2021). In particular, projections of future AMOC changes are very sensitive to model-simulated mean state and internal variability of AMOC (Weijer et al. 2020; Ma and Jiang 2023). However, our limited understanding of the AMOC internal variability, and how that might evolve as a consequence of global warming, remains one of the largest sources of uncertainty in near-term future AMOC projections (Roberts and Palmer 2012; Roberts et al. 2014; Reintges et al. 2017; Jackson et al. 2022).

It has long been recognised that AMOC is highly variable on a range of timescales—from days to millennia (Robson et al. 2016; Jackson et al. 2019; Srokosz et al. 2021; Megann et al. 2021). Numerous studies have demonstrated

✉ Jon Robson
j.i.robson@reading.ac.uk

1 National Centre for Atmospheric Science, Reading, UK

2 Department of Meteorology, University of Reading, Reading, UK

3 Met Office Hadley Centre, Exeter, UK

4 Present Address: National Oceanography Centre, Southampton, UK

5 NSF National Center for Atmospheric Research, Boulder, USA

Published online: 31 January 2024

that AMOC multidecadal variability is a major driver of the North Atlantic sea surface temperature (SST) changes (Zhang et al. 2019). That is, the AMOC plays an important role in the Atlantic multidecadal variability (AMV) which modulates wide-ranging atmospheric and oceanic processes. The link between AMOC and AMV, as well their implications for wider weather and climate systems, provide long-term predictability of the climate in the broad North Atlantic region (Smith et al. 2020) and beyond. Nonetheless, such predictability relies upon the accurate simulation of AMOC in climate models that is compromised by many factors including model parameterisations (Marshall et al. 2017), model biases (Heuzé 2017), and coupling with other components of the Earth system (Kostov et al. 2019). For example, the Coupled Model Intercomparison Project (CMIP) Phase 5 models have large spread in AMOC multidecadal variability which is mostly underestimated compared to observations (Yan et al. 2018; Xu et al. 2019). Compared to CMIP5, there are significant advances in the latest generation CMIP6 models (Eyring et al. 2016). For example, it is reported that CMIP6 models are closer to observed interannual AMOC variability compared to CMIP5 (Kelson et al. 2022). Yet, CMIP6 models still present significant uncertainty and bias in characterising the mean state and variability of AMOC (Weijer et al. 2020).

A recent study by Lai et al., (2022) reported significant differences in the simulation of AMV between two versions of the UK Met Office models made for CMIP6 (HadGEM3-GC3.1-LL and HadGEM3-GC3.1-MM). They found that such differences are associated with the representation of AMOC related to model resolution and many other processes. Particularly, HadGEM3-GC3.1-LL lacks AMOC meridional coherence and the depth-space subsurface density anomalies in this model are confined to the subpolar latitudes. However, it is unclear whether the difference in AMOC is specific to the HadGEM3 model, or whether it is resolution-specific or other factors contribute. To address these questions, we take advantage of five models that have similar ocean configurations within CMIP6. Specifically, they are three non-UK models (CNRM-CM6-1, EC-Earth3, IPSL-CM6A-LR) and two UK models (HadGEM3-GC31-LL and UKESM1-0-LL). We aim to characterise model diversity in simulating AMOC multidecadal variability, latitudinal coherence, as well as the processes driving such differences. To preclude the impact of externally forced changes, we analyse the preindustrial control (piControl) experiment (Table 1) made for CMIP6.

While the nature of AMOC internal variability remains an open question, there is increasing evidence that buoyancy-forced surface water mass transformation (WMT) in the Subpolar North Atlantic (SPNA) plays a critical role (Kim et al. 2020; Yeager et al. 2021). That is, the transformation of warm, light surface waters along the northward upper limb of the overturning into cold, dense North Atlantic deep water (NADW) in high-latitude regions is believed to sustain AMOC and its variability. However, the relative roles of SPNA subregions in this mechanism remain unclear (Yeager et al. 2021). For example, Zhang and Thomas (2021) argued that WMT in the Arctic plays more important role in sustaining AMOC, whereas WMT in Labrador and Greenland seas have long been thought to be the key driver of AMOC change. Here, we employ WMT analysis to explore important processes that might explain model differences in simulating AMOC internal variability.

The paper is structured as follows. In Sect. 2, we briefly introduce models and data used in this work, as well as the computations of the AMOC and WMT in density space and the WMT analysis. We characterise AMOC mean states and

**Table 1** The 5 NEMO-based climate models used in this study

| Model | CNRM-CM6-1 | IPSL-CM6A-LR | EC-Earth3 | HadGEM3-GC31-LL | UKESM1-0-LL |
|---|---|---|---|---|---|
| variant | r1i1p1f2 | r1i1p1f1 | r2i1p1f1 | r1i1p1f1 | r1i1p1f2 |
| Ocean grids (ni × nj × nLevel) | 362 × 294 × 75 | 362 × 332 × 75 | 362 × 292 × 75 | 362 × 332 × 75 | 362 × 332 × 75 |
| Isoneutral mixing coefficient | 1000 $m^2\ s^{-1}$ | | | | |
| Vertical mixing scheme | Turbulent Kinetic Energy (TKE) + internal wave-induced mixing parameterization of de Lavergne et al. (2019), including tidal | | TKE + a double diffusive mixing parameterization; a tidal mixing parameterization has been added to OPA of de Lavergne et al. (2019) | TKE | |
| Atmospheric model | ARPEGE-Climat 6.3 | LMDZ6 | IFS | GA7.1 | GA7.1 |
| Sea ice model | Gelato 6 | LIM3.6 | LIM3 | CICE | CICE |
| Model reference | Voldoire et al. (2019) | Boucher et al., (2020) | Döscher et al., (2021) | Kuhlbrodt et al. (2018) | Sellar et al., (2019) |

For each model, we analyse the first 500 years of one ensemble member (i.e., variant) from the CMIP6 piControl experiment

multidecadal variability across models in Sect. 3 and 4. We then explore the links between surface WMT and AMOC diversity in Sect. 5. Important processes behind model differences are analysed in Sect. 6 and summarised in Sect. 7. Our major findings are summarised and discussed in Sect. 8.

## 2 Data and methods

### 2.1 Models and simulations

We examine the representation of the AMOC in five CMIP6 climate models (Table 1). All the five models use the Nucleus for European Modelling of the Ocean (NEMO) version 3.6 (NEMO3.6) with ORCA1 grid as their ocean models. Note however that other component models, such as the atmosphere and sea ice, are model-dependent. The ORCA1 grid has 75 vertical levels and a nominal horizontal resolution of around 1° that is refined to around 1/3° around the equator and polar regions. Also, there are small differences in the bathymetry across models, which leads to differences in the representation of overflow transport across the Scotland-Greenland ridge. To focus on the AMOC internal variability, we analyse the CMIP6 preindustrial control (piControl) simulation. The piControl experiment employs fixed pre-industrial era (i.e., 1850 here) external forcings including solar, land use, greenhouse gases, etc. To accommodate the different simulation lengths across models, we only analyse the first 500 years from each model.

Of the five models, two are from the UK Met Office – the physical climate model HadGEM3-GC31-LL and the Earth system model UKESM1-0-LL. These two models share the same physical–dynamical core (Sellar et al. 2020). For example, they employ the same atmosphere (i.e., Global Atmosphere 7.1 (GA7.1)) and sea ice (i.e., Los Alamos Sea Ice Model (CICE)) models. The atmosphere has a horizontal resolution of approximately 135 km and 85 levels with a model lid at 85 km above sea level. Major differences between HadGEM3-GC31-LL and UKESM1-0-LL revolve around the addition of more Earth system processes and couplings in the latter (Sellar et al. 2019). For example, UKESM1-0-LL has interactive treatments of ocean heat and carbon uptake, carbonate chemistry, and ocean biology. For simplicity, we refer these two models as the "UK models" hereinafter.

In addition to the two UK models, we also analyse three other fully-coupled climate models that also use NEMO3.6 as their ocean model component. CNRM-CM6-1 was jointly developed by the Centre National de Recherches Météorologiques (CNRM) and Cerfacs (Voldoire et al. 2019). The atmospheric component of CNRM-CM6-1 is based on version 6.3 of the global atmospheric model ARPEGE-Climat. It has a horizontal resolution of about 1.4° at the equator and 91 vertical levels up to 0.01 hPa. Sea ice within CNRM-CM6-1 is represented by Gelato 6 (Voldoire et al. 2019). EC-Earth3 is an Earth System Model developed collaboratively by the European research consortium EC-Earth (Döscher et al. 2021). It consists of the atmosphere model IFS and the sea ice module LIM3. The atmosphere model adopts a linearly reduced Gaussian grid equivalent to $512 \times 256$ longitude/latitude (approximately 0.7° at the equator) and 91 levels in the vertical (up to 0.01 hPa). Finally, IPSL-CM6A-LR is the low resolution (LR) version of the IPSL-CM6A model (Boucher et al. 2020). It employs LMDZ6 as its atmospheric model and LIM3.6.for sea ice. The atmosphere has a horizontal resolution of $1.25° \times 2.5°$ and 79 levels in the vertical (up to 1 Pa). We refer to these three models as the "non-UK models" hereafter.

### 2.2 Observations and reanalysis

The observation-based SST analysis from the Hadley Centre Sea Ice and Sea Surface Temperature (HadISST; Rayner et al. (2003)) is used here. We compare HadISST 1871–1950 climatological mean with piControl following Lai et al., (2022). We note however that model-to-observation biases are insensitive to the climatological period selected. We also use the 1901–1950 ocean temperature and salinity data from version 4.2.2 of the Met Office Hadley Centre "EN" series (EN4; Good et al. (2013)) to calculate sea water density and compare to those from CMIP6 piControl. It should be noted that there is very limited observational dataset being integrated in the EN4 dataset for the period 1901–1950, and this is particular the case for the Arctic (Good et al. (2013)).

### 2.3 Computation of metrics

We calculate seawater density offline using the Thermodynamic Equation of Seawater–2010 (TEOS-10) referenced to the pressure level 2000 dbar, i.e., Sigma2. We choose Sigma2 for direct comparison to AMOC calculated in density space using Sigma2, which has the advantage to better characterize deep water masses over large areas. We acknowledge that Sigma2 quantitatively differs slightly from Sigma0 due to non-linear components involved in the definitions. However, the results and conclusions of this study are not sensitive to such differences. The temperature-driven component of density evolution is calculated using the same equation but using time-varying monthly mean temperature while holding the salinity at their monthly climatological means and vice versa for the salinity-driven density evolution (Lai et al. 2022).

We present AMOC in density (Sigma2) space unless otherwise denoted. Density-space AMOC is computed by integrating basin-wide meridional volume transport as a function of isopycnals following Menary et al. (2020b). Specifically,

densities are regridded onto velocity grids and the overturning is calculated by summing volume transports along the line and then summing cumulatively in density space. Also, following Menary et al. (2020b), we do not apply compensation term to remove the impact of a non-zero net transport along a given latitude for the reasons discussed therein. We present AMOC strength primarily using the maximum of overturning streamfunction at 45°N (AMOC45) in density space—defined at the isopycnal where the climatological maximum of the overturning at 45°N occurs (hereinafter as Sigma_amoc45). We also present the overturning at 65°N and 60°N using the same method where applicable. To avoid confusion, we hereinafter refer the whole SPNA AMOC as overturning, and AMOC at Sigma_amoc45 as AMOC45. We define the lower limb of the overturning as the density classes above (i.e., denser than) the Sigma_amoc45, and the upper limb as density classes below (i.e., lighter than) the Sigma_amoc45.

We compute the AMV index as the area average of linearly detrended SST over North Atlantic region (0°N–90°N, 75°W–15°E) following Lai et al. (2022).

We calculate surface forced WMT by integrating the surface density flux (freshwater flux plus heat flux) over the outcropping region for a given isopycnal following Langehaug et al. (2012) and Yeager et al. (2021). Additionally, we compute WMT driven by surface density variations using the same method but with time-varying monthly mean surface temperature and salinity while holding surface heat and freshwater fluxes at their monthly climatological means. Similarly, we calculate surface flux driven WMT using time-varying monthly mean surface heat and freshwater fluxes while holding surface temperature and salinity at their monthly climatological means (Petit et al. 2021). The surface WMT is integrated for the whole SPNA region as well as regional basins defined in Figure S1. The regional seas include: the Labrador Sea (LAB) that is demarcated by the western section of the OSNAP campaign; the Irminger–Iceland Basin (IIB) enclosed by the western section of the OSNAP campaign and the lines along the Sills; the western subpolar gyre (WSPG) that includes the LAB and the south-western part of the subpolar gyre; Eastern subpolar gyre (ESPG) that includes the IIB and the south-eastern part of the subpolar gyre; the Greenland–Iceland–Norwegian seas (GIN); and the Arctic Ocean (ARC) north of the GIN Seas, including the Barents Sea.

To calculate the Greenland-Scotland Ridge overflow transport (GSRO) along the Greenland-Iceland sills (Sills),, we first extract vertical profiles of volume transport along the Sills line; the line is defined along vorticity points of the Arakawa C grid. We use this line to extract volume fluxes (both meridional and zonal) on their natural grid points in order to preserve the model transports. These transports are regridded into density space. For more details, please refer to Jackson et al. (2020) and Jackson and Petit. (2022). We then define the overflow by integrating water masses denser than 36.8 kg $m^{-3}$ in density space following (Petit et al. 2021). Finally, we compute GSRO as the sum up of overflow water denser than 36.8 kg $m^{-3}$ across the Denmark strait, the Iceland–Fareo channel, and the Fareo–Scotland channel.

For all indices defined above, we compute their low-frequency component using a 15-year moving mean and refer to the 15-year smoothed data as multi-decadal variability. To assess the statistical significance of the relationship between time series (i.e., cross correlation and lagging regression), we apply the 15-year block bootstrap method following Lai et al. (2022). To avoid the impact of model drifts on regressions, we perform linear detrending to all metrics before statistical analysis.

## 3 Models' mean state and bias

Before comparing the variability of the overturning and the mechanisms that control it, we first compare the mean state of the models.

Figure 1a1–e1 show that all the NEMO models are cold-biased in the broad SPNA region compared to HadISST. This is most pronounced in the subpolar gyre with a cold bias of up to − 6 K in all models. Sea-ice covered areas are masked off in this comparison. The cold bias is a common issue in low-resolution models due to the representation of the North Atlantic Current that is too weak and too zonal (Danabasoglu et al. 2014). Meanwhile, there is a warm bias along the northern edge of the ESPG in UK models. The top 100 m are generally too fresh in all models compared to EN4 in the broad SPNA region, and particularly in the central subpolar gyre (Fig. 1 a2–e2). However, all models simulate a too saline Gulf stream, Iceland basin, and the seas along the coast of UK and Norway; this is also a common feature of low-resolution models associated with a too weak AMOC. Notably, salinity bias in the Arctic shows a distinct contrast between the UK and non-UK models. Here, non-UK models are too saline while the UK models are too fresh (also see Figs. S2 and S3).

The annual mean climatology of the top 500 m mean density (Fig. 1 a3–e3) shows a similar spatial pattern across models, featuring a relatively denser WSPG compared to the ESPG. Meanwhile, the GIN Seas stand out as the densest region of the whole North Atlantic in all models. It is important to note the Arctic features a lighter upper ocean sea water (Figs. 1d3, e3) along with a deeper (around 100 m) mixed layer (Fig. S2a1) in the UK models compared to non-UK models. This is consistent with the model-simulated upper ocean salinity that is fresher in the Arctic in the UK models. A careful comparison between the spatial pattern of upper ocean salinity bias to upper ocean density climatology

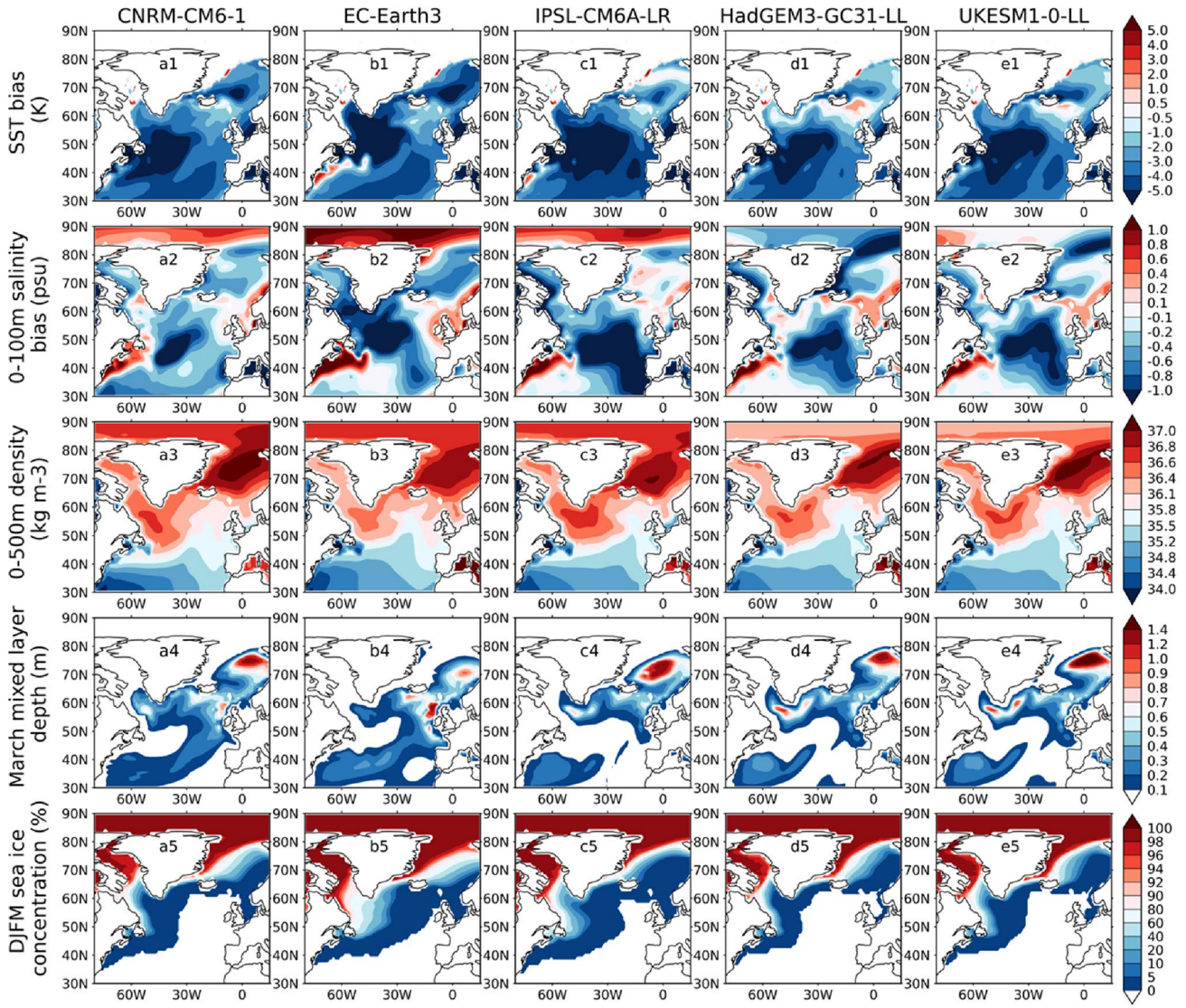


**Fig. 1** Model mean state and bias. a1–e1 Annual mean SST bias (K) compared to HadISST (1871–1950 mean). a2–e2 0–100 m annual mean sea water salinity bias (psu) compared to EN4 (1901–1950 mean). a3–e3 Climatological mean of top 500 m annual mean density (Sigma2; kg $m^{-3}$). a4–e4 Climatological mean of March mixed layer depth climatology (km). a5–e5 Climatological mean of the winter (December–March) mean sea ice concentration (%)

reveals the dominant role of salinity in the distribution of upper ocean sea water density in all models. This is consistent with the fact that the upper ocean stratification is dominated by the salinity distribution in the broad SPNA region in all models as well as in EN4 (Fig. S2).

Wintertime deep convection is strongest in the GIN Seas in all models, yet the strength and centres of the deep convection regions differ across models (Fig. 1 a4–e4). There are considerable differences in winter convection in the LAB across models. For instance, UK models show deeper LAB convection compared to non-UK models. The EC-Earth3 model (Fig. 1b4) has the weakest convection in LAB likely related to excessive sea ice coverage there (Fig. 1b5), but stronger convection in the Iceland basin compared to all other models. Over the Arctic, the differences in the mixed layer depth mean state is generally small, but there is a noticeable difference in the multidecadal variability of the mixed layer depth with EC-Earth3 having significantly more variability than the other models (Fig. S4).

Models show a wide range of the mean states of the SPNA overturning in both density-space (Fig. 2a1–e1) and depth-space (Fig. S5). In density-space, the basin-wide time-mean overturning strength increases from subtropical to subpolar latitudes, peaking between 55°N and 60°N. The basin-wide overturning is strongest in CNRM-CM6-1 (Fig. 2a1) and weakest in IPSL-CM6A-LR (Fig. 2c1). This is also

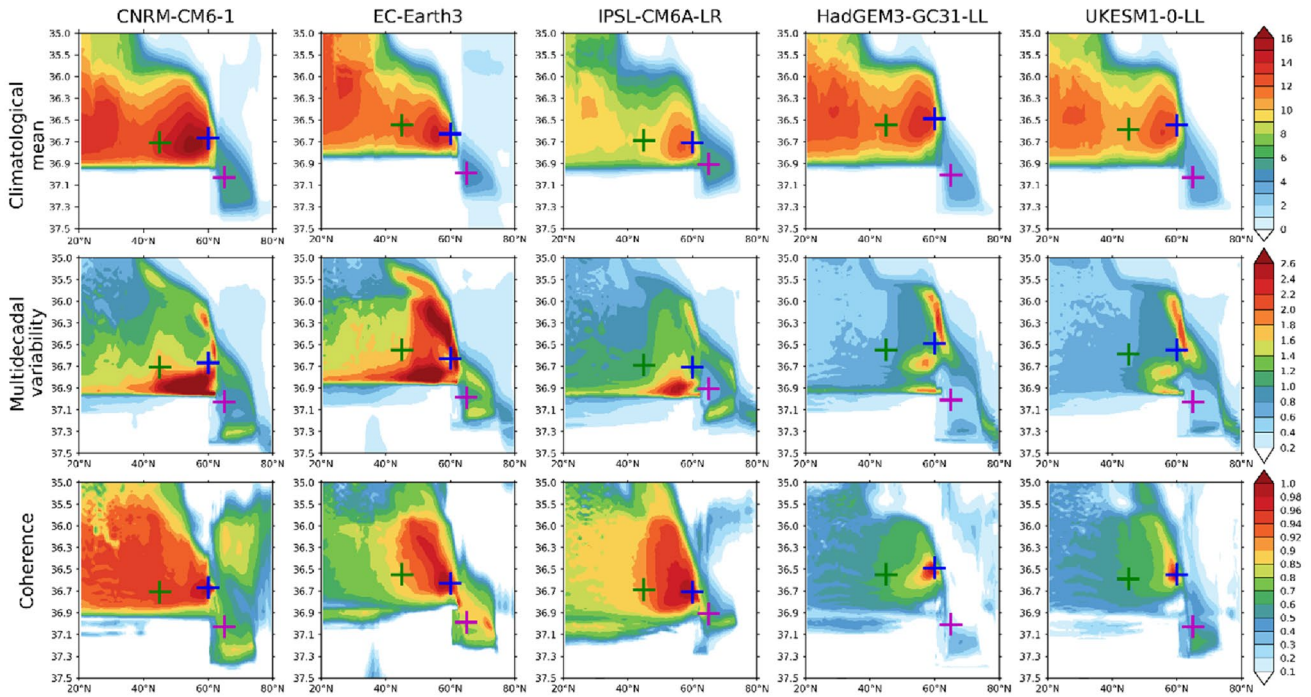


**Fig. 2** Mean state, multidecadal variability, and coherence of the annual mean AMOC stream function (Sv) as a function of density (Sigma2; *y*-axis; kg $m^{-3}$) and latitude (*x*-axis). The top row shows the climatological mean. The second row shows the standard deviation of 15-year running mean of annual mean AMOC. The third row shows the instantaneous correlation between AMOC and low-frequency AMOC60. The density layers at which the climatological maximum of AMOC at 45°N, 60°N, and 65°N are shown in each model and denoted by, respectively, the green, blue, and purple pluses

shown by the maximum overturning at 45°N (i.e., AMOC45 in Figs. 3a, b), where IPSL-CM6A-LR is weakest (about 9 Sv) while CNRM-CM6-1 is strongest (about 14 Sv). In addition to the basin-wide overturning, there is also a subpolar overturning cell (55°N–60°N) that is prominent in all models. However, the magnitude of the subpolar cell, and the density classes over which it resides, varies significantly across models. It is important to note that the lower limb of the overturning spans a wider range of density classes in UK models (i.e., it is more diffuse). For instance, the maximum overturning at 60°N (blue plus signs) and 45°N (green plus signs) occur in lighter classes (Fig. 2d1, e1) in UK than in non-UK models. North of the subpolar latitudes, there is an overturning cell above 37.0 kg $m^{-3}$ corresponding to overturning in the GIN Seas that is around 1.3–1.9 times stronger in non-UK models compared to UK models.

## 4 Diversity in the variability and latitudinal coherence of AMOC

In this section, we characterise the multi-decadal variability and latitudinal coherence of the AMOC in density-space, focusing on the diversity across models (Figs. 2, 3, 4). Figure 3a shows the time series of AMOC45 measured at Sigma_amoc45. The five NEMO models show very different simulations of the magnitude, timescale, and variability of AMOC45. The UK models show substantially smaller magnitude AMOC45 multidecadal variability (Fig. 3a, b). As consistent with AMOC45, the time series of AMV also shows pronounced difference between UK and non-UK models, with much larger variability in the latter (Fig. 3c, d). The AMOC45 variability has a broadly consistent impact on the North Atlantic sea surface temperatures across models, with increased AMOC45 associated with basin-wide warming (Fig. 3e). However, the UK models show weaker AMV variations while non-UK models, and particularly EC-Earth3, show larger AMV variations associated with multidecadal AMOC45 variations (Fig. 3f). Such differences between UK and non-UK models are consistent with the weaker AMOC45 variability in UK models.

Figures 2a2–e2 show the multidecadal variability of the overturning in density space. The structure of the multidecadal variability shows considerable difference to that of mean overturning (Fig. 2a1–e1). In particular, the largest variability tends to occur at different isopycnals and latitudes compared to that of the mean state. Specifically, in non-UK models, the largest variability generally occurs in the lower limb where waters are denser than Sigma_amoc45 (i.e., around 36.7 kg $m^{-3}$ as denoted by the green crosses).

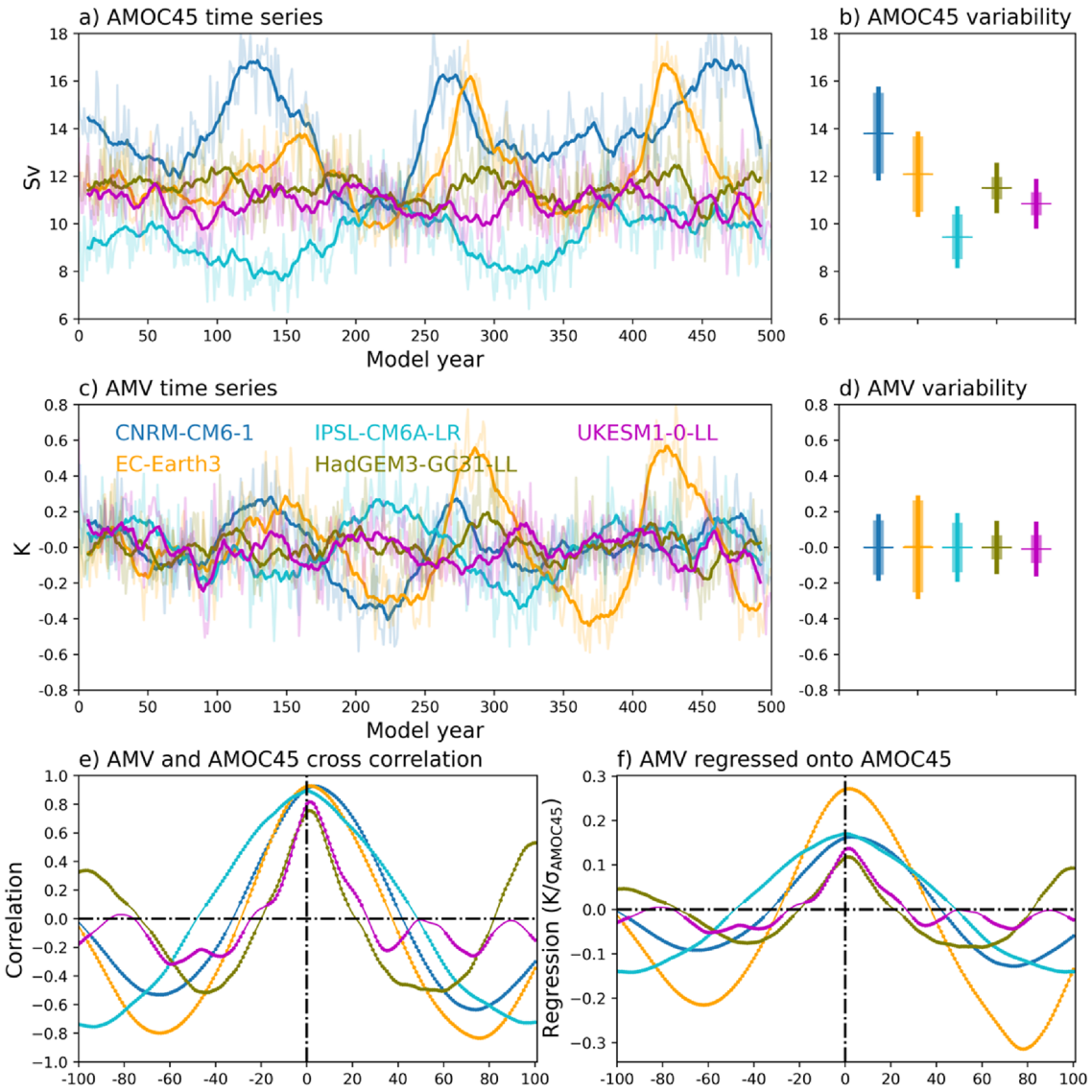


**Fig. 3** AMOC45 and AMV. **a** Time series of annual mean (thin lines) and 15-year running mean (thick lines) AMOC45, **b** AMOC45 interannual (thin vertical bar) and multidecadal (15-year running mean; thick vertical bar) variability measured by standard deviation. **c**, **d** The same as **a**, **b**, but for AMV. Horizontal bars in **b**, **d** show the climatological mean states. **e** cross correlation and **f** lead-lag regression of AMV onto normalised low-frequency (15-year running mean) AMOC45. AMOC45 leads AMV to the right of the x-axis in number of years. Solid circles in **e**, **f** denote statistical significance at the $p \leq 0.05$ level based on a two-sided Monte Carlo test

Note that EC-Earth3 (Fig. 2b2) presents large variance in both the upper and lower limbs. Overall, in non-UK models, the largest variability is found at the layer where the largest variation in the deep western boundary current is found (Yeager et al. 2021). In contrast, the UK models show smaller variability at all latitudes (Fig. 2d2, e2), as has also been seen in the time series of AMOC45 (Fig. 3a, b). In the UK models, there are also three distinct cells of large variance that reside in different density layers. This includes two distinct cells of prominent variance in the dense limb (i.e., around 36.7 and 36.9 kg $m^{-3}$), whilst the highest variance is found in the upper limb spanning the density classes of 36.2–36.5 kg $m^{-3}$. In non-UK models, however, the two cells of large variance in the lower limb seem to be merged into one, implying a possible entrainment of the deep sea overflow water. Such entrainment of deep water seems to be either too weak or missing in the UK models.

Along with the difference in the multidecadal variability of the overturning, UK models also show weaker latitudinal coherence of the overturning. First, Fig. 2a3–e3 show that there is a weaker correlation between AMOC60 and the overturning at lower latitudes. This suggests a weaker link between subtropical and subpolar overturning in UK models. Indeed, the UK models lack the latitudinal

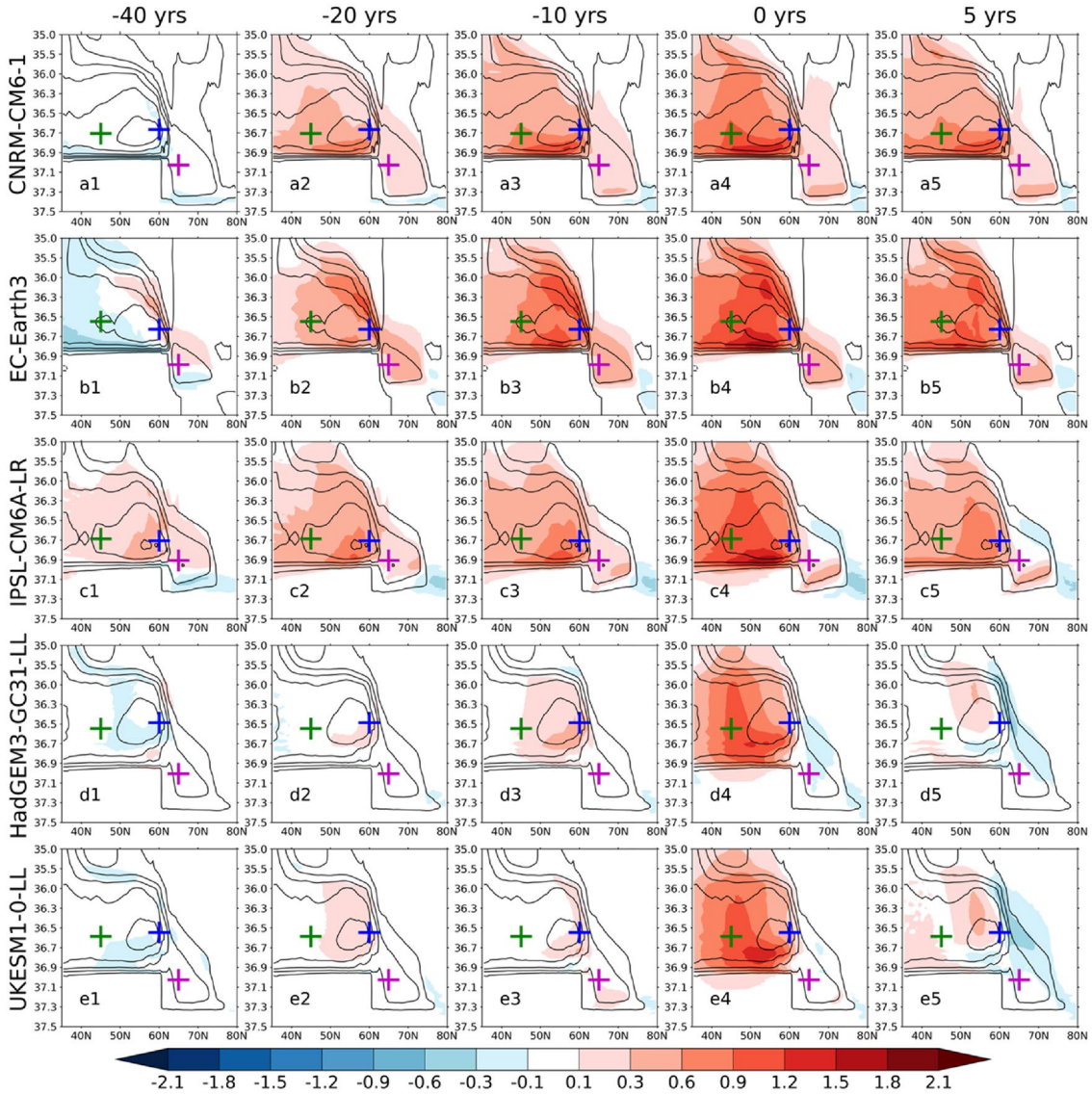


**Fig. 4** Propagation of the overturning anomalies in density space (Sigma2; *y*-axis; kg $m^{-3}$). Contours show the climatological mean of annual mean AMOC stream function while colours show regression of the overturning onto AMOC45 ($Sv/\sigma_{AMOC45}$). From left to right are respectively 40, 20, 10, 0 years before and 5 years after AMOC45. The density layers at which the climatological maximum of AMOC at 45°N, 60°N, and 65°N are denoted by, respectively, the green, blue, and purple pluses

coherence of overturning circulation in density-space as seen in non-UK models (Figs. 4 and S6). Albeit a weaker signal in CNRM-CM6-1, the lower limb anomalies start generally from high-latitudes and then propagate slowly southward to subtropical regions in all non-UK models. These anomalies then propagate to the upper limb and persist. However, in UK models (bottom two rows in Fig. 4), the anomalies are confined to the subpolar gyre and do not propagate meridionally to subtropical regions over time and the AMOC45 changes show a much weaker link to previous overturning anomalies at high latitudes.

The weak latitudinal coherence of the overturning circulation in UK models is consistent with the fact that the subsurface (1500–2500 m) density anomalies do not propagate along the western boundary in UK models (bottom two rows in Fig. 5). In contrast, there is a clear southward propagation of the subsurface density anomalies along the western boundary over time in non-UK models (Top three rows in Fig. 5). In addition to the weak latitudinal coherence of subsurface density anomalies, the GIN Seas density anomalies also show a weak link with density anomalies south of the Sills and lower latitudes in UK models. This is

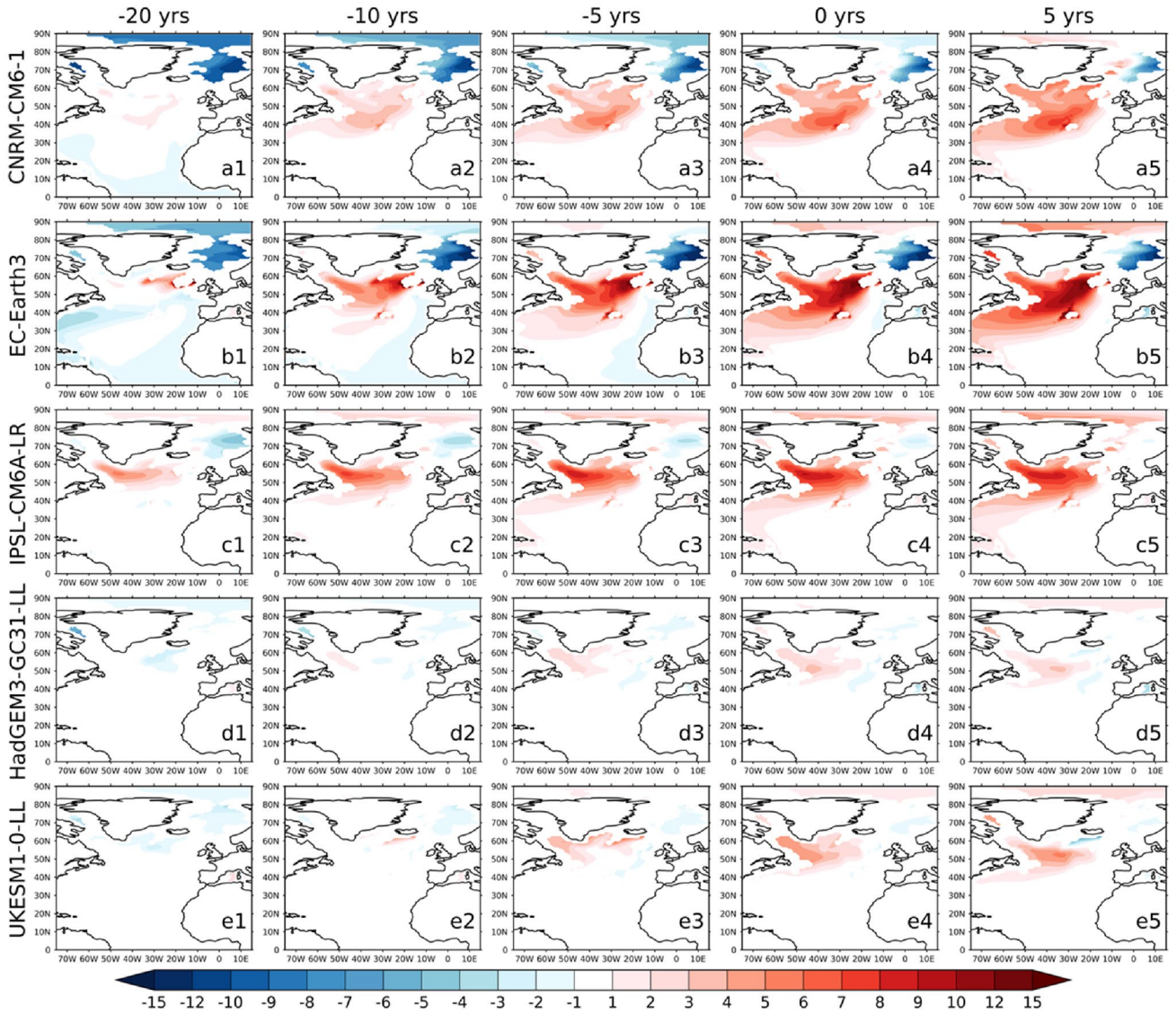


**Fig. 5** Propagation of deep layer (1500–2500 m) density anomalies associated with the normalised low-frequency (15-year running mean) AMOC45 (kg $m^{-3}/\sigma_{AMOC45}$). From left to right are respectively 20, 10, 5, 0 years before and 5 years after AMOC45

consistent with the overturning anomalies that seem to be disconnected between the subpolar gyre and the GIN Seas in the UK models (Fig. 4).

Despite the differences, the above analysis shows that the density-space overturning anomalies consistently start from the lower dense limb at high latitudes in all the five models. This is supported by the finding that multidecadal variability of AMOC45 is dominated by the variability in the lower dense limb rather than the level where the maximum overturning occurs in density space across models (Figs. 6 and S7). The dominance of the lower dense limb in the multidecadal variability of the overturning is consistent with Yeager et al. (2021). More specifically, the lower dense limb of the overturning at 45°N leads the AMOC45 index (measured at Sigma_amoc45). Meanwhile, changes in the upper limb lag the AMOC45 index (Fig. 6). It is, however, noted that there are clear differences between UK and non-UK models in the magnitude, timescale, and variability of the lower dense limb of the overturning.

The diversity in the timescale of the lower limb overturning shown in Fig. 6 is in line with Fig. 3 which shows diversity in the timescale of AMOC45 across models. We also note that the timescale of AMOC in non-UK models features a strong multi-centennial variability, as have also been reported by Jiang et al. (2021) and Meccia et al. (2023). This is in clear contrast to UK models where the centennial AMOC variability is absent.

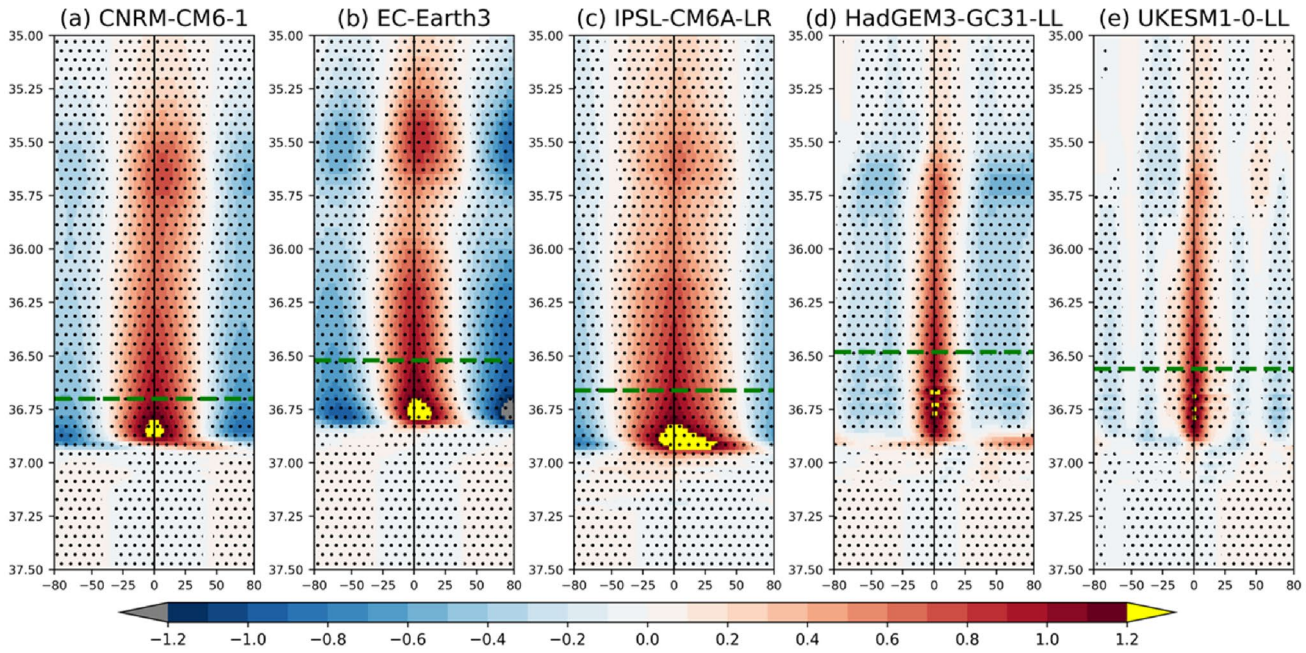


**Fig. 6** Lead-lag regression of density-space overturning at 45°N onto the normalised low-frequency (15-year running mean) AMOC45 index (Sv/σAMOC45). The horizontal green lines denote the density layer where the climatological maximum overturning at 45°N (AMOC45) occur in each model. Density-space overturning at 45° leads AMOC45 index to the left. Dotted stippling denotes statistical significance at the $p \leq 0.05$ level based on a two-sided Monte Carlo test. *Y*-axis is the density (Sigma2; kg $m^{-3}$) coordinate, and *x*-axis denotes number of years before and after AMOC45 peaks

## 5 Surface water mass transformation and links to the variability of the overturning

To explore processes that underpin the differences in the lower dense limb of the overturning and thereby differences in the variability and coherence between UK and non-UK models, we turn to WMT analysis in this section. We primarily use the AMOC45 index to explore the relationship between the overturning and WMT over the broad SPNA region North of 45°N (including the whole Arctic Ocean). Figure 7a shows that there is a strong link between multidecadal AMOC45 variations and changes in the SPNA-integrated WMT that is averaged across density bins. This justifies the usage of surface WMT analysis for understanding the multidecadal variability of the overturning circulation. We also note that the link between AMOC and WMT is in line with Desbruyères et al. (2019), and has been analytically established by Swingedouw et al. (2019). It is clear, however, that the WMT changes associated with AMOC45 show substantial difference between UK and non-UK models (Fig. 7b). That is, the WMT anomalies associated with AMOC45 are significantly weaker in the UK models. This is consistent with the finding that UK models have weaker magnitude variability and latitudinal coherence of the overturning.

The climatological mean of SPNA-integrated annual mean WMT peaks around 36.5 kg $m^{-3}$ in non-UK models (Fig. 7c–e). However, the UK models (Fig. 7f–g) show three peaks spanning the light-density classes (around 35.3–35.8 kg $m^{-3}$), the intermediate-density classes (around 36.3 kg $m^{-3}$), as well as the high-density classes (around 36.9 kg $m^{-3}$). This is consistent with the diffuse lower limb of the overturning circulation in UK models shown in Fig. 2. For WMT integrated over high-density classes above 36.5 kg $m^{-3}$, the climatology mean state shows similar spatial pattern and magnitude across models (top rows in Figs. 8 and S8): that is, most high-density WMT occurs in the GIN Seas, with consistent WMT in the Norwegian Seas in most models and to a lesser extent from IIB and LAB. This is also seen in Fig. 7c–g which confirm that the GIN Seas dominate SPNA high-density WMT in all models. We note that the Arctic WMT in UK models (Figs. 7f, g), primarily in light-density classes, is much stronger compared to non-UK models that have most of the WMT in high-density classes. In contrast to the similar spatial pattern and magnitude of the mean state of high-density classes WMT, the multidecadal variability of WMT integrated over high-density classes shows significant difference between UK and non-UK models (bottom rows in Figs. 8 and S8). That is, the multidecadal variability of high-density WMT in UK models is much weaker. Indeed, Figs. 7k, l show that the UK models

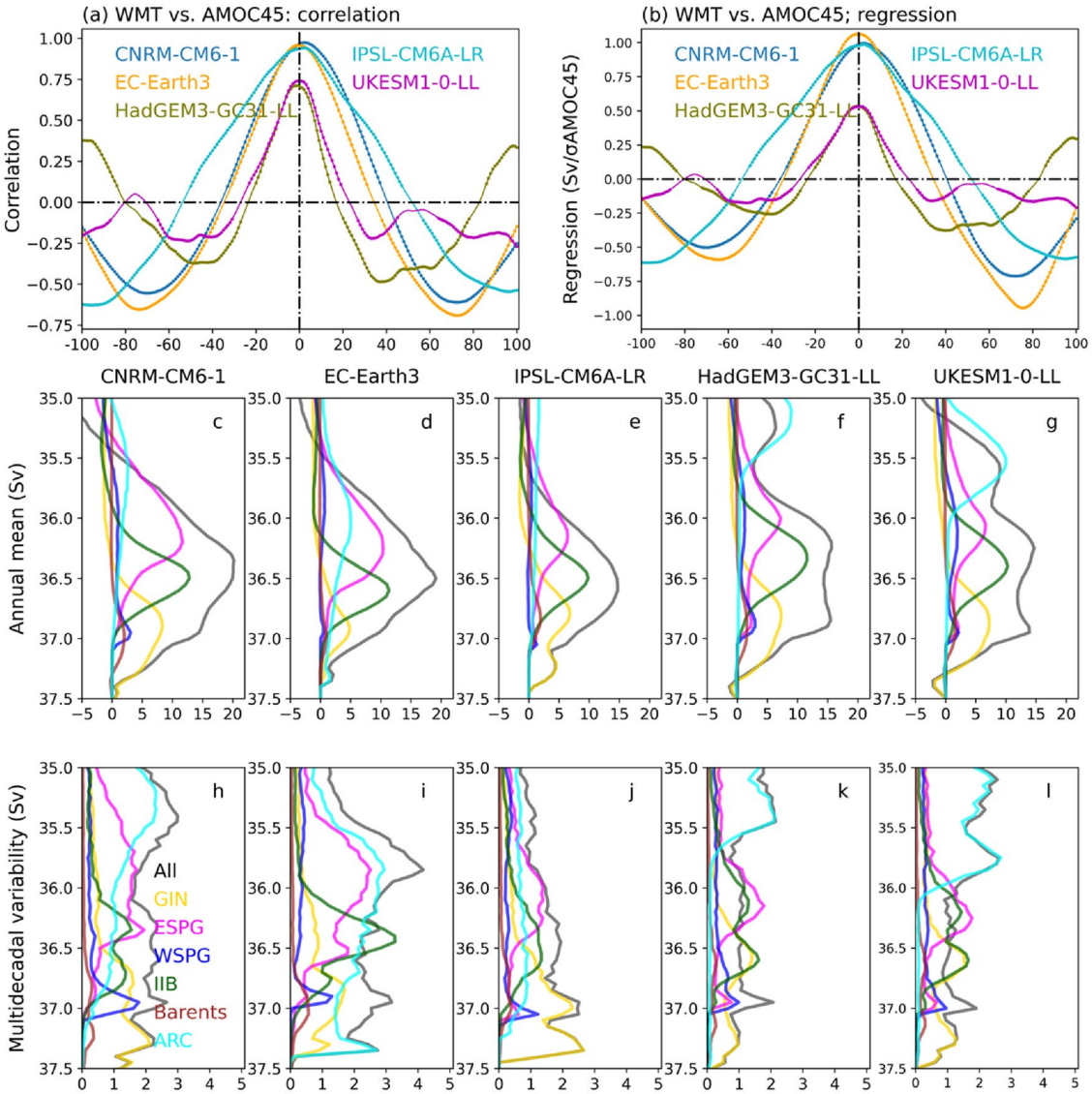


**Fig. 7** Relationship between AMOC45 and water mass transformation (WMT) in the broad subpolar North Atlantic (SPNA; including the Arctic). **a** cross correlation and **b** lead-lag regression (Sv/$\sigma_{AMOC45}$) of SPNA integrated WMT (averaged across all density bins) onto normalised low-frequency (15-year running mean) AMOC45. WMT leads AMOC45 to the left and lags to the right of the *x*-axis by years. The second row shows the climatological mean of annual mean WMT (*x*-axis, Sv) integrated over SPNA as a function of Sigma2 (*y*-axis; kg $m^{-3}$). Also shown are the decompositions into regional seas: the Greenland-Iceland-Norwegian Seas (GIN; yellow), Eastern Subpolar Gyre (ESPG; magenta), Western Subpolar gyre (WSPG, blue), Irminger sea – Iceland basin (IIB; green), Barents Sea (Barents; brown), and the Arctic (ARC; cyan). The third row is the same as the second row, but for multidecadal variability of annual mean WMT. Solid circles in **a**, **b** denote statistical significance at the $p \leq 0.05$ level based on a two-sided Monte Carlo test

feature much stronger light-density variability in the Arctic but much weaker high-density variability in the GIN Seas and the Arctic.

The above implies that the weaker multidecadal variability of the overturning circulation is associated with weaker changes in SPNA high-density WMT in the UK models, and particularly of those generated in the Arctic and GIN Seas. To further understand this, we examine SPNA WMT anomalies associated with multidecadal AMOC45 variations, focusing on the contributions from different basins of the SPNA region (Fig. 9a1–e1). We first note that increased WMT at high-density classes consistently leads the AMOC45 in all models. We stress again this is consistent with the finding that the AMOC45 multidecadal variability is dominated by lower dense-limb variability rather than by the variability of the maximum overturning (Fig. 6). It is also worth noting that the WMT in ESPG lags AMOC45 in most models as denoted by the pink contours

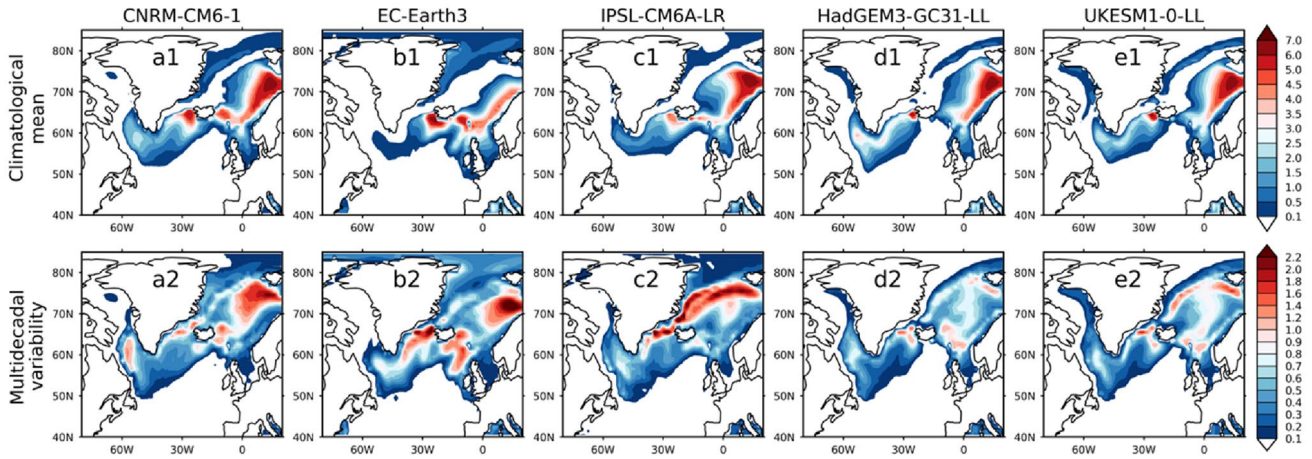


**Fig. 8** Climatological mean and multidecadal (15-year running mean) variability of water mass transformation (WMT) flux (m $m^{-2}$ $day^{-1}$) integrated above 36.5 kg $m^{-3}$

in Fig. 9 which shows the ESPG dominates WMT following a peak in AMOC. This link between WMT in ESPG and the AMOC45 had also been reported in the Community Earth System Model (Yeager et al. 2021). Although the location of increased WMT is model dependent, changes in the GIN Seas appear to be important in all models with additional roles for LAB in the high-density changes. That is, increased WMT in high-density classes in GIN Seas clearly leads AMOC45. However, the role of the GIN Seas appears to be smaller both in terms of magnitude and persistence in the UK models (Fig. 9d1, e1).

The Arctic also appears to play an important role in the variability of the overturning in non-UK models. Specifically, increased WMT in the Arctic, as denoted by the cyan contours in Fig. 9 which shows the Arctic dominates WMT prior to the peak in AMOC, leads the AMOC45 in all models and appears to pre-condition GIN Seas WMT at denser water mass classes in non-UK models. That is, in non-UK models, increases in high-density WMT in the Arctic is leading increases in the GIN Seas WMT in even higher density classes. This is particularly important in the EC-Earth3 model that sees the most prominent high-density WMT in the Arctic. As a result, there are increases in lower-limb density anomalies that lead AMOC45 increases. However, such preconditioning (i.e., high-density class WMT in the Arctic leading to further high-density class WMT in the GIN Seas) is absent in the UK models; in these models the Arctic WMT occurs in much lighter water masses and the Arctic WMT is disconnected from dense waters.

The importance of WMT in the Arctic and GIN Seas over high-density classes in non-UK models is supported by their projections on the GSRO shown in Fig. 10a, b, where the GSRO shows strong projection on AMOC65. By contrast, in UK models, high-density class WMT in Arctic and GIN Seas has very limited influence on the GSRO. The readers are referred to Fig. S8 for the same analysis but for WMT separated between the Arctic and the GIN Seas in Fig. S9. This is consistent with the fact that the multidecadal variability of GSRO in the UK models (around 0.2 Sv) is much weaker compared to that in the non-UK models (around 0.6–0.8 Sv). A possible hypothesis is that internal diapycnal mixing between light water masses transformed in the Arctic and dense water masses transformed in GIN Seas might be weakening the influence (Fig. 9). This might be related to the mean state of mixed layer depth and convection in the GIN Seas due to different mixing schemes employed in the UK models (Table 1), and we suggest an in-depth examination of this for future work. Consistently, the GSRO shows a weaker projection on AMOC45 in UK models compared to non-UK models (Fig. 10c, d). We notice the different lags in the projections. However, we are not clear about the processes shaping such differences, and this could be a focus for further research.

In short, our analysis above demonstrates a clear link between the low frequency variability of the overturning and high-density class WMT in GIN Seas and the Arctic. This link is much stronger in non-UK models than in UK models. This is also consistent with the differences in the latitudinal coherence of the overturning between UK and non-UK models.

## 6 Drivers of surface water mass transformation changes

Given the close link between high-density WMT in the Arctic and GIN Seas and the variability of the overturning circulation, it is necessary to understand the drivers of WMT changes in these regions. The WMT variations associated with low-frequency AMOC45 (Fig. 9 top row)

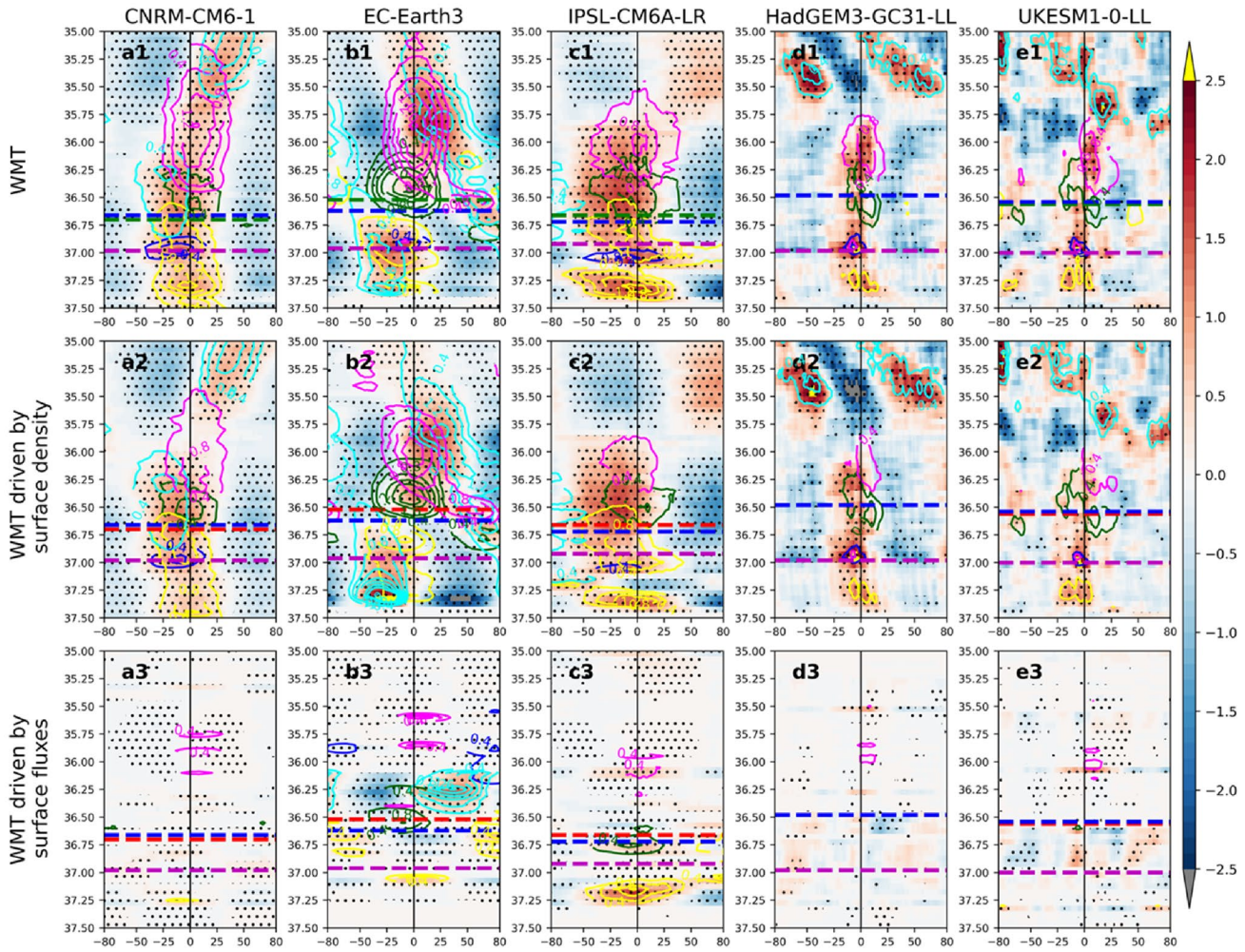


**Fig. 9** Density space WMT anomalies associated with low-frequency (15-year running mean) AMOC45. (a1–e1) regression (Sv $Sv^{-1}$) of WMT onto AMOC45. Colours for WMT integrated over the broad SPNA region, while contours show WMT anomalies for different sub-sea regions: cyan for the Arctic, yellow for the GIN Seas, blue for the Western Subpolar gyre (WSPG), pink for the Eastern Subpolar gyre (ESPG), and green for the Irminger sea-Iceland basin (IIB). Horizontal dashed lines denote the density layer where the climatological maximum AMOC at 65°N (purple), 60°N (blue), and 45°N (green) occur respectively. AMOC45 leads to the right and lags to the left. (a2–e2) same as (a1–e1), but for WMT calculated using climatological mean heat and freshwater fluxes and monthly varying surface density. (a3–e3) same as (a1–e1), but for WMT calculated using monthly varying heat and freshwater fluxes and climatological mean surface density. Dotted stippling denotes statistical significance at the $p \leq 0.05$ level based on a two-sided Monte Carlo test

are predominately driven by variations in surface density (Fig. 9 middle row) rather than variations in surface fluxes (Fig. 9 bottom row) in the whole SPNA region in all models. This is consistent with Petit et al. (2021) and Årthun (2023) who found that surface WMT variations over the subpolar gyre region is dominated by surface density variations using observational datasets. We therefore conclude that model differences in surface densification processes are critical drivers of differences in high-density WMT and hence difference in the variability of the overturning circulation between UK and non-UK models. As such, we further explore the drivers of surface density changes. We found that the SPNA sea surface density variation is primarily driven by changes in surface salinity in all models (Fig.S10). For example, in the GIN Seas, surface density variation is primarily driven by surface salinity changes that is partially counteracted by changes in surface temperature (Fig. 11). Meanwhile, in the Arctic, surface density variation is almost entirely driven by surface salinity changes (Fig. S11). Note the variability of surface density in both the Arctic and GIN Seas are much smaller in UK models than non-UK models, and see smaller influence of salinity variations.

Sea surface salinity in the Arctic and GIN Seas can change due to various processes. For instance, changes in atmospheric forcing, meridional transport of salinity and freshwater from the Atlantic, and subsurface processes.

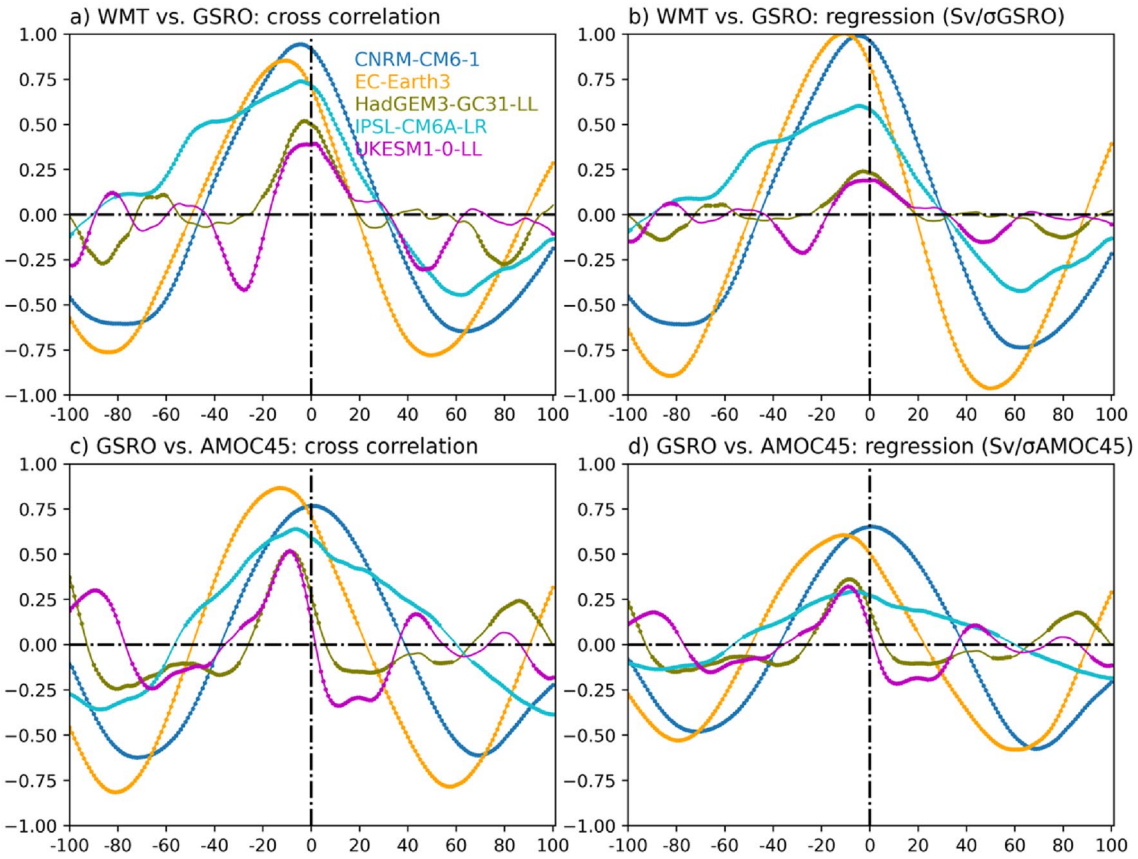


**Fig. 10** Relationship between Arctic + GIN Seas WMT and AMOC. **a** Cross correlation and **b** Lead-lag regression of WMT (Sv) integrated above 36.8 kg $m^{-3}$ in the Arctic and GIN Seas onto normalised low-frequency (15-year running mean) Greenland-Scotland Ridge overflow (GSRO; Sv). WMT leads the GSRO to the left and lags to the right of the *x* axis by years. **c** Cross correlation and **d** lead-lag regression of GSRO onto normalised low-frequency (15-year running mean) AMOC45. GSRO leads AMOC to the left and lags to the right of the *x*-axis. Solid circles denote statistical significance at the $p \leq 0.05$ level based on a two-sided Monte Carlo test

Jiang et al. (2021) found that in the IPSL-CM6A-LR model, salinity/freshwater exchanges between the Arctic and GIN Seas play crucial roles in the multidecadal variability of the overturning. Also, Lai et al. (2022) found that upper-ocean salinity-controlled density anomalies from the Arctic appear to be driving subsurface density anomalies in the subpolar region in HadGEM3-GC3.1-LL. Motivated by these findings, we examine the importance of the Arctic in overturning diversity across models. We found a strong anti-correlation between the Arctic and GIN Seas surface density evolutions (Figs. 12a and S12) that is dominated by surface salinity variations (Figs. 12b and S13). Specifically, GIN Seas surface density/salinity anomalies gradually build up on multidecadal timescales as surface density/salinity in the Arctic decline. This suggests that the Arctic and GIN Seas salinity exchanges plays an important role in driving GIN Seas surface salinity anomalies. We therefore examined salinity transport anomalies along the East Greenland Current (EGC) associated with multidecadal AMOC45 variations. We found that salinity anomalies along the EGC lead AMOC45 in all models, while there are significant differences in the strength of the relationship between UK and non-UK models (Fig. 12c). By contrast, anomalies in the strength of the EGC lag AMOC45 (Fig. 12d), while there is not much difference in the EGC strength anomalies associated with AMOC45 between UK and non-UK models, and the lag of largest regressions coefficients is model dependent. Therefore, salinity changes in the GIN Seas appear to be related to the advection of salinity anomalies along the EGC out of the Arctic Ocean. However, in the UK models, salinity anomalies propagating out of the Arctic appear to be weaker and therefore have a smaller impact on surface density and WMT.

To further investigate the importance of salt transport from Arctic for high-density class WMT in the GIN Seas, we turn to salt and heat transport into the GIN Seas including northward transports from the Atlantic across the sills (top row in Fig. 13) and southward transports from the Arctic across the Fram Strait (bottom row in Fig. 13). We see that salt transport into the GIN Seas clearly leads WMT

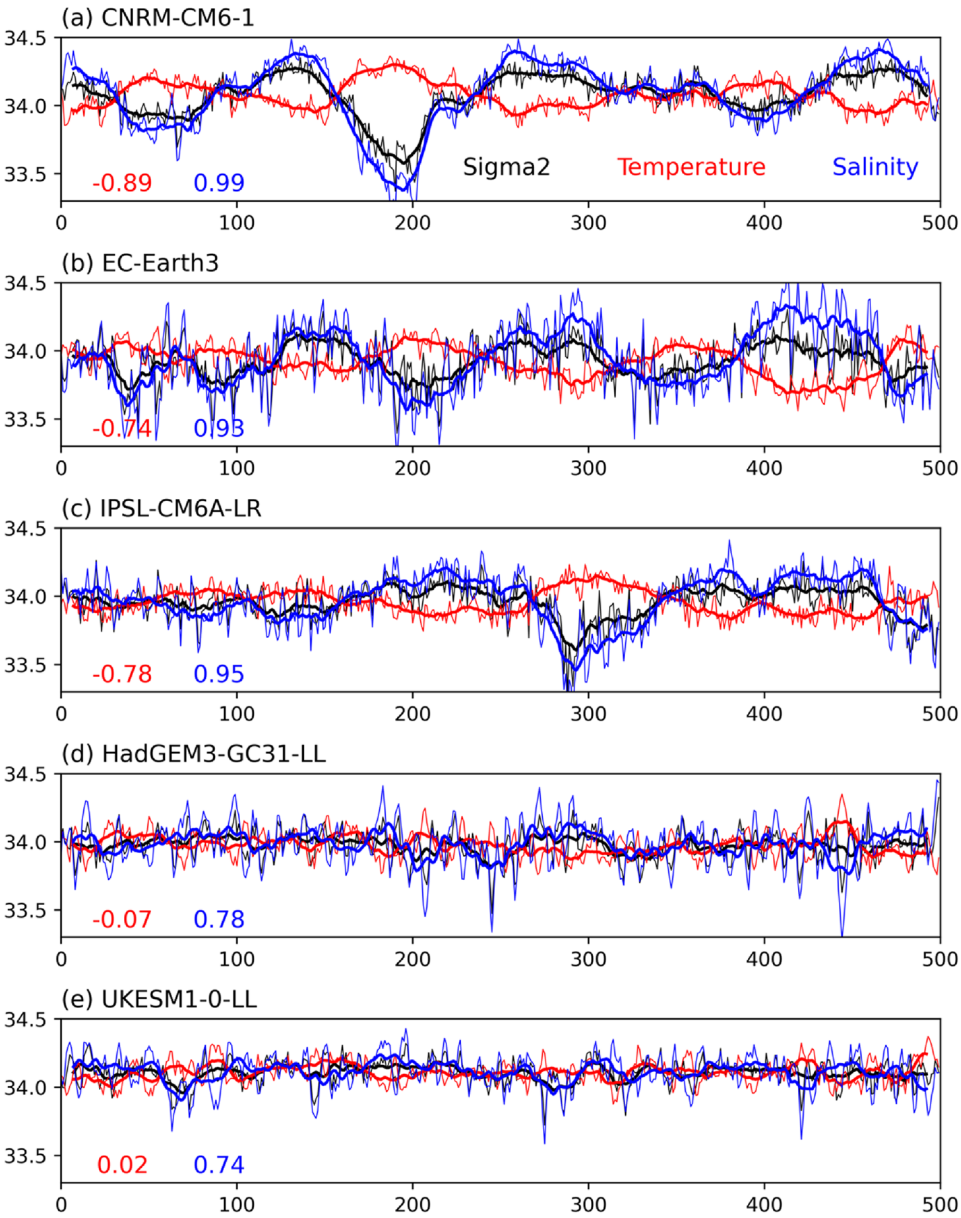


**Fig. 11** Time series of GIN Seas area-weighted annual mean sea surface density (sigma2; kg $m^{-3}$). Black for Sigma2 calculated using monthly varying sea surface temperature and salinity, blue (red) for salinity (temperature) driven Sigma2 variations. Thin lines are for annual mean, while solid lines are for 15-year running mean. Numbers at the bottom left corner of each panel denote the correlation between 15-year running mean Sigma2 and temperature (red) and salinity (blue) driven Sigma2 variations

there. However, salt transport from the Atlantic has a weaker relationship with high-density class WMT compared to that from the Arctic. More importantly, it is the southward salt transport from the Arctic that both leads WMT and shows a clear difference between UK and non-UK models in its relationship to WMT. Furthermore, although the heat transport (Fig. 13b) into GIN Seas from the Atlantic is related to WMT, it does not consistently lead the WMT across models. Increased heat transport into the GIN Seas can also not explain the dominant role of increased surface density in WMT anomalies (Fig. 9). Hence, this analysis again supports our conclusion that the salinity anomalies advected from the Arctic plays a critical role in shaping the diversity in the variability of WMT in the GIN Seas and, hence, the diversity in AMOC multidecadal variability.

While the drivers of model bias in the Arctic remain unclear, the representation of sea ice processes is likely to play an important role. Indeed, in all models, surface freshwater fluxes associated with sea ice changes dominate WMT variability in the Arctic, and significantly cancel out surface heat fluxes driven WMT in the GIN Seas (not shown). Therefore, the different sea ice schemes employed in different models, as well as their responses to atmospheric forcing and oceanic processes, might be a driver of model diversity in AMOC. Also, the slightly different representation of the Greenland-Scotland Ridge bathymetry and overflow might also play a role. Further, Lai et al. (2022) concluded that atmospheric circulation anomalies in the Arctic do not have significant impact on salinity anomalies propagating out of the Arctic in the HadGEM-GC3.1-LL model, we do

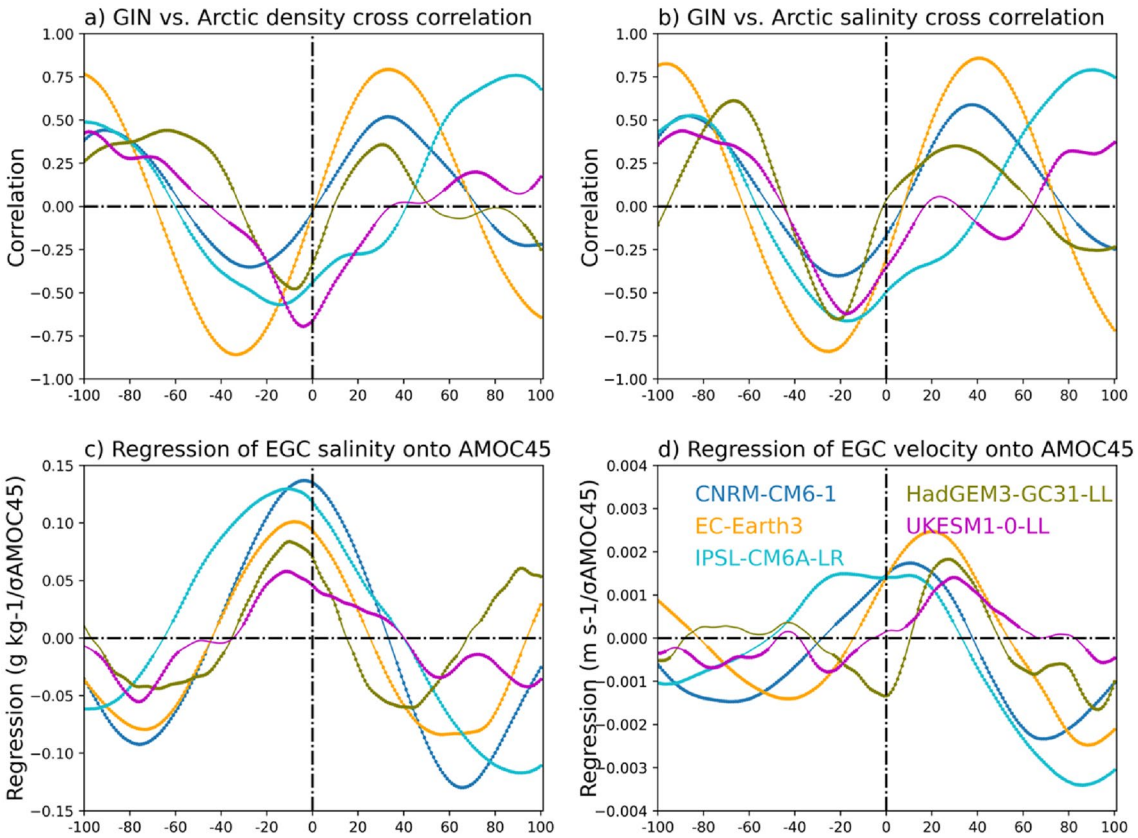


**Fig. 12** Link between the Arctic and the GIN Seas surface density anomalies. **a** cross correlation between the GIN Seas and Arctic area-weighted 0–500 m mean low-frequency (15-year running mean) density (Sigma2; kg $m^{-3}$). **b** The same as **a**, but for salinity (So; g $kg^{-1}$). The Arctic leads GIN Seas to the right and lags to the left. **c** regression (g $kg^{-1}/\sigma_{AMOC45}$) of salinity anomalies along the East Greenland Current (EGC, defined as southward flows over the region of 65°N–80°N, 25°W–5°W) onto normalised low-frequency (15-year running mean) AMOC45. **d** The same as **c**, but for anomalies in the southward current (m $s^{-1}/\sigma_{AMOC45}$). AMOC45 leads to the right and lags to the left of the *x*-axis in **c**, **d**. Solid circles denote statistical significance at the $p \leq 0.05$ level based on a two-sided Monte Carlo test

not know if, and how, atmospheric circulation anomalies are coupled with Arctic-Atlantic salinity exchanges across models.

## 7 Summary of the mechanism driving difference in AMOC variability and discussion

Figure 14 shows a schematic summarising our proposed mechanism explaining differences in the variability of the overturning between UK and non-UK models. We stress the dominant role of model-simulated mean state of the Arctic and the GIN Seas surface salinity in sea surface density variations for high-density class WMTs in these regions. Meanwhile, we highlight the importance of salinity-governed surface density exchanges between the Arctic and GIN Seas for driving AMOC variations on multidecadal time scales in these NEMO-based climate models. This reveals the crucial importance to further understand processes driving surface salinification/densifications in these regions and whether they are realistic representations of low-frequency variability.

Model bias in the ocean surface mean states plays a strong role in AMOC variability and coherence. Particularly, UK models simulate a fresher Arctic which is linked to the weaker salinity exchanges between the Arctic and GIN Seas via the EGC. Further, the model bias in surface salinity also appears to impact WMT: the relatively weak WMT in the Arctic over high-density classes in the UK models is explained by too fresh surface water that reduces the outcropping area associated with high-density classes. We also note that salt transport from the Arctic leads GIN Seas WMT by 10–20 years in Fig. 13c. However, it is not clear what governs this timescale. Thus, more work is needed to understand how temperature and salt transport changes salinity and density budgets in the GIN Seas.

The overall weaker AMOC variability in the UK models is consistent with a range of processes such as a relatively weaker AMOC meridional coherence, weaker high-density

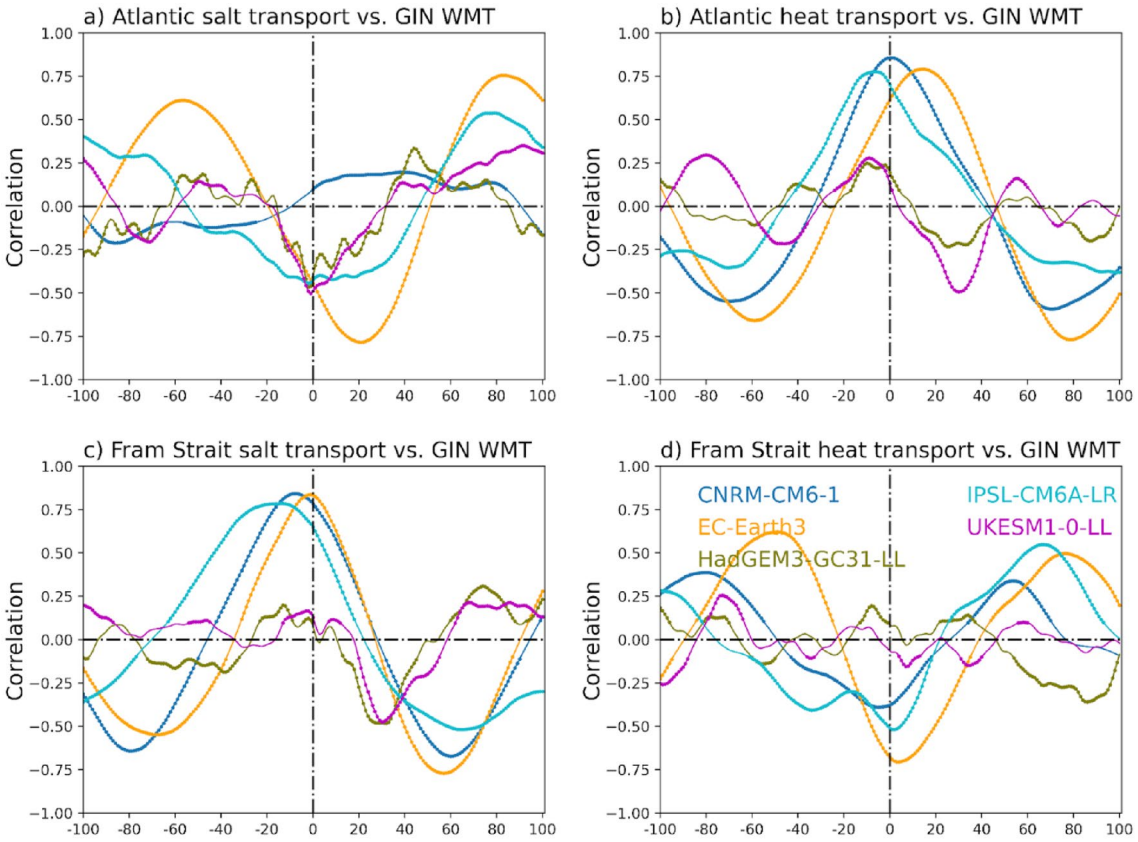


**Fig. 13** Cross correlation between inflow salt (left) and heat (right) transport from the Atlantic (northward) and across the Fram strait (southward). WMT lags to the left of the x-axis and leads to the right of the *x*-axis. Solid circles denote statistical significance at the $p \leq 0.05$ level based on a two- sided Monte Carlo test

class WMTs, and a weaker magnitude and persistence of salinity anomalies in the Arctic and GIN Seas. However, it is not clear if, and how, these processes influence each other. For instance, are surface salinity changes in the GIN Seas associated with AMOC latitudinal coherence? Although Jiang et al., (2021) concluded that the meridional salt/freshwater transport plays a minor role in salinity changes in GIN Seas and the Arctic in the IPSL-CM6A-LR model, it is necessary to understand if that is also the case for all the NEMO-based models analysed here.

It is worth stressing the prominent multi-centennial variability of AMOC in the IPSL-CM6A-LR (Jiang et al. 2021) and EC-Earth3 (Meccia et al. 2023) models. This has also been reported by paleo-climate studies (e.g., Laepple and Huybers, 2013; Ayache et al. 2018). Such multi-centennial variability of AMOC is also found here in the CNRM-CM6-LR model (Figs. 3 and 6). Nonetheless, the magnitude of such variability differs among the three non-UK models. The UK models, by contrast, do not show a very strong multi-centennial variability of the AMOC. Jiang et al. (2021) and Meccia et al. (2023) reached a similar conclusion that the multi-centennial variability of AMOC is tied with the accumulation of freshwater/salinity anomalies over the Arctic and their release to the North Atlantic, and therefore impact deep water mass formation and AMOC variability. We note that this is in agreement with our WMT analysis and conclusion that surface density exchange between the Arctic and the GIN Seas are critical for AMOC variability in the five NEMO-based climate models analyzed here.

Finally, it is important to stress that the AMOC lower dense limb in the UK models is very diffuse. This might be due to internal mixing of water masses formed in different density classes in different regions. For example, there appears to be a stronger mixing downstream of the overflow water at 65°N, which is particularly seen in the IIB region in the UK models (green contours between the blue and purple dashed lines Figs. 9). As a result, the maximum overturning at 45°N occurs in much lighter water masses than non-UK models (Fig. 2). However, we acknowledge the challenges in investigating these processes in the low-resolution models analysed here and recommend further studies using high-resolution models in which diapycnal mixing associated processes are better resolved.

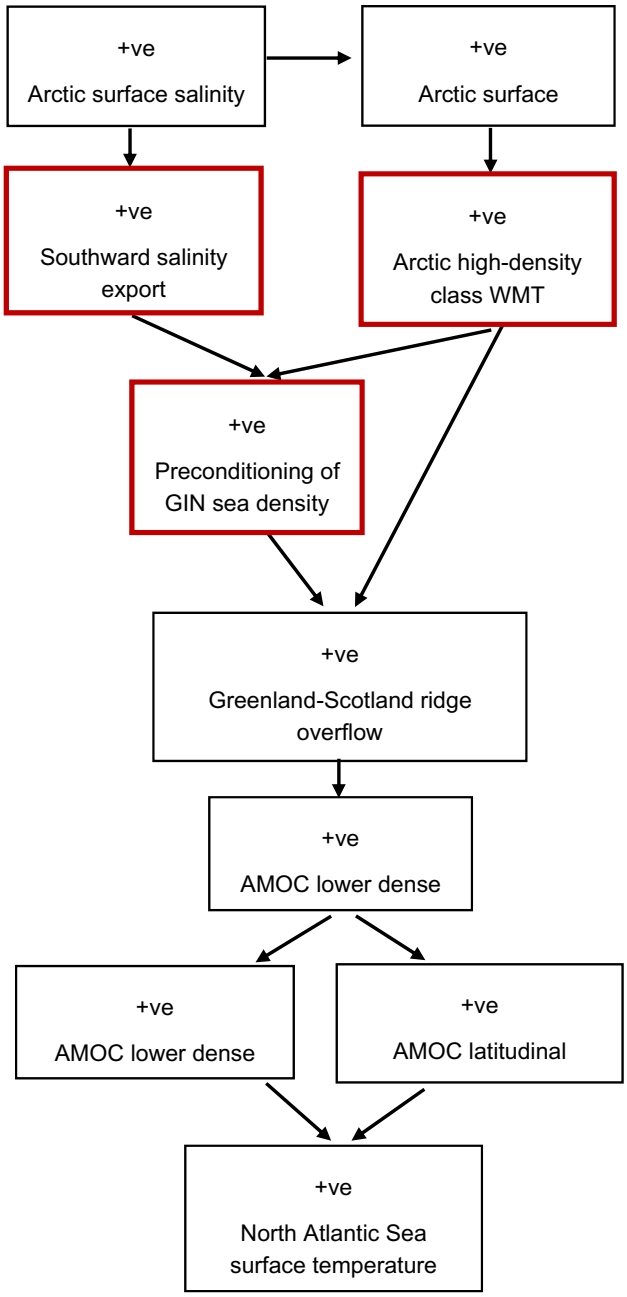


**Fig. 14** Schematic of proposed mechanism explaining the difference in AMOC variability between UK and non-UK models. Arrows indicate pathways where positive impact are active. Red outlines highlight key processes weak or missing in the UK models

## 8 Conclusions

In this study, we characterise multidecadal AMOC internal variability in 5 low-resolution (i.e., 1° ocean) fully coupled models that all use the NEMO3.6 ocean model. We have analysed the CMIP6 preindustrial control simulations, and have taken the surface water mass transformation (WMT) framework to explore important processes that might be driving diversity in AMOC variability across models. The key results are as follows:

- Large diversity is found in the simulation of the timescale, multidecadal variability, and latitudinal coherence of the AMOC across NEMO-based models. Particularly, the UK models show substantially smaller magnitude AMOC multidecadal variability and weaker latitudinal coherence compared to the non-UK models, and the AMOC lower limb spans a wider range of density classes (i.e. it is more diffuse).
- The AMOC multidecadal variability has consistent impact on the North Atlantic sea surface temperatures across models, with increased AMOC leading to warming. However, the Atlantic Ocean sea surface temperatures variation associated with multidecadal AMOC variability is smaller in the UK models than in non-UK models, which is consistent with the weaker AMOC variability and latitudinal coherence in the UK models.
- In density space, multidecadal AMOC variability at 45°N is dominated by variability in the lower dense limb of the AMOC, rather than that at the isopycnal of "maximum" overturning. This is consistent with the fact that increased WMT at higher density classes (above 36.8 kg $m^{-3}$) consistently leads the maximum AMOC at 45°N in all the models.
- High-density class WMT changes in the GIN Seas appear to be an important driver of the lower dense limb AMOC in all models with additional roles for Labrador Sea. However, the role of the GIN Seas appears to be smaller (in magnitude and persistence) in the UK models.
- The Arctic appears to play an important role in the AMOC variability in non-UK models. In particular, increased high-density class Arctic WMT leads AMOC45 and appears to pre-condition WMT at denser water mass classes in the GIN Seas. However, such high-density WMT in the Arctic and the GIN Seas preconditioning is missing in UK models.
- In all models the WMT changes that lead AMOC45 are dominated by salinity-governed surface density anomalies rather than changes in surface heat or freshwater fluxes.
- Surface salinity changes in the GIN Seas show strong relationship with the advection of salinity anomalies out of the Arctic ocean. However, in the UK models, salinity anomalies propagating out of the Arctic are much weaker and are consistent with smaller impacts on surface salinity in the GIN Seas.

In short, even though the same NEMO3.6 model is used in the five models analysed here, we found large diversity in models' simulated AMOC multidecadal variability and latitudinal coherence. This underlines the sensitivity of the

AMOC to model details. We found that salinity-governed surface densification processes in the Arctic and GIN Seas are key in driving AMOC variability and the diversity across these models. Given that we expect large changes in WMT and overturning in the Arctic and GIN seas regions as global warming continues (Lique and Thomas 2018; Asbjørnsen et al. 2023) it is important to better understand salinity and density budgets in these regions for more reliable projections of AMOC changes. It is also interesting to explore whether, and how, differences in the importance of these regions across models lead to differences in AMOC projections. Therefore, we recommend further in-depth studies to better understand and constrain processes driving salinity changes in these regions for more reliable representations of the AMOC in climate models.

**Supplementary Information** The online version contains supplementary material available at https://doi.org/10.1007/s00382-023-07069-y.

**Acknowledgements** We acknowledge the World Climate Research Programme, which, through its Working Group on Coupled Modelling, coordinated and promoted CMIP6. We thank the climate modeling groups for producing and making available their model output, the Earth System Grid Federation (ESGF) for archiving the data and providing access, and the multiple funding agencies who support CMIP6 and ESGF. This work used JASMIN, the U.K. collaborative data analysis facility. We thank Laura Jackson from Met Office for providing tools and insights for this study. We thank the two anonymous reviewers for their interest and comments on this paper.

**Funding** This study was funded by the NERC WISHBONE project (NE/T013516/1, NE/T013540/1). JR and TP were additionally funded by the NERC SNAP-DRAGON project (NE/T013494/1). JR, RS and JM were funded via the NERC CANARI (NE/W004984/1) project. JR and RS also acknowledge funding from UKRI via the EPOC project. SY acknowledges support from US National Science Foundation (NSF) grant 2040020 (NSF WISHBONE).

**Data availability** The CMIP6 model data used in this study were downloaded from the ESGF (e.g., https://esgf-index1.ceda.ac.uk/) and are freely available. References for the simulations used are in Table 1. HadISST data are available at https://www.metoffice.gov.uk/hadobs/hadisst/. The Twentieth Century Reanalysis (20CR) data are available at https://www.esrl.noaa.gov/psd/.

**Declaration**

**Conflict of interest** The authors declare no conflict of interest.



## References

Årthun M (2023) Surface-forced variability in the Nordic Seas overturning circulation and overflows. Geophys Res Lett 50:e2023GL104158. https://doi.org/10.1029/2023GL104158

Asbjørnsen H, Årthun M (2023) Deconstructing future AMOC decline at 26.5°N. Geophys Res Lett 50:e2023GL103515. https://doi.org/10.1029/2023GL103515

Ayache M, Swingedouw D, Mary Y, Eynaud F, Colin C (2018) Multi-centennial variability of the AMOC over the Holocene: A new reconstruction based on multiple proxy-derived SST records. Glob Planet Change 170:172-189. https://doi.org/10.1016/j.gloplacha.2018.08.016

Bakker P et al (2016) Fate of the Atlantic meridional overturning circulation: strong decline under continued warming and greenland melting. Geophys Res Lett 43:12252–12260. https://doi.org/10.1002/2016GL070457

Bellomo K, Angeloni M, Corti S, von Hardenberg J (2021) Future climate change shaped by inter-model differences in Atlantic meridional overturning circulation response. Nat Commun 12:3659. https://doi.org/10.1038/s41467-021-24015-w

Boucher O et al (2020) Presentation and evaluation of the IPSL-CM6A-LR climate model. J Adv Model Earth Syst 12:e2019MS002010. https://doi.org/10.1029/2019MS002010

Danabasoglu G (2014) North atlantic simulations in coordinated ocean-ice reference experiments phase II (CORE-II). Part I Mean States Ocean Model 73:76–107. https://doi.org/10.1016/j.ocemod.2013.10.005

Döscher R et al (2021) The EC-earth3 earth system model for the climate model intercomparison project 6. Geosci Model Dev Discuss. https://doi.org/10.5194/gmd-2020-446

Eyring V, Bony S, Meehl GA, Senior CA, Stevens B, Stouffer RJ, Taylor KE (2016) Overview of the coupled model intercomparison project phase 6 (CMIP6) experimental design and organization. Geosci Model Dev 9:1937–1958

Good SA, Martin MJ, Rayner NA (2013) EN4: quality controlled ocean temperature and salinity profiles and monthly objective analyses with uncertainty estimates. J Geophys Res Oceans 118:6704–6716. https://doi.org/10.1002/2013JC009067

T Hassan, Allen RJ, Liu W, Randles C (2020) Anthropogenic aerosol forcing of the AMOC and the associated mechanisms in CMIP6 models. Dynamics/Atmospheric Modelling/Troposphere/Physics (physical properties and processes).

Heuzé C (2017) North Atlantic deep water formation and AMOC in CMIP5 models. Ocean Sci 13:609–622. https://doi.org/10.5194/os-13-609-2017

Hu A, Roekel LV, Weijer W, Garuba OA, Cheng W, Nadiga BT (2020) Role of AMOC in transient climate response to greenhouse gas forcing in two coupled models. J Clim 33:5845–5859. https://doi.org/10.1175/JCLI-D-19-1027.1

Jackson LC, Petit T (2022) North Atlantic overturning and water mass transformation in CMIP6 models. Clim Dyn. https://doi.org/10.1007/s00382-022-06448-1

Jackson LC et al (2019) The mean state and variability of the north atlantic circulation: a perspective from ocean reanalyses. J Geophys Res Oceans 124:9141–9170. https://doi.org/10.1029/2019JC015210

Jackson LC et al (2020) Impact of ocean resolution and mean state on the rate of AMOC weakening. Clim Dyn 55:1711–1732. https://doi.org/10.1007/s00382-020-05345-9

Jackson LC, Biastoch A, Buckley MW, Desbruyères DG, Frajka-Williams E, Moat B, Robson J (2022) The evolution of the north atlantic meridional overturning circulation since 1980. Nat Rev Earth Environ. https://doi.org/10.1038/s43017-022-00263-2

Jiang W, Gastineau G, Codron F (2021) Multicentennial variability driven by salinity exchanges between the atlantic and the arctic

ocean in a coupled climate model. J Adv Model Earth Syst 13:e2020MS002366. https://doi.org/10.1029/2020MS002366
Kelson RL, Straub DN, Dufour CO (2022) Using CMIP6 models to assess the significance of the observed trend in the Atlantic meridional overturning circulation. Geophys Res Lett 49:e2022GL100202. https://doi.org/10.1029/2022GL100202
Kim WM, Yeager S, Danabasoglu G (2020) Atlantic multidecadal variability and associated climate impacts initiated by ocean thermohaline dynamics. J Clim 33:1317–1334. https://doi.org/10.1175/JCLI-D-19-0530.1
Kostov Y, Johnson HL, Marshall DP (2019) AMOC sensitivity to surface buoyancy fluxes: the role of air-sea feedback mechanisms. Clim Dyn 53:4521–4537. https://doi.org/10.1007/s00382-019-04802-4
Kuhlbrodt T, Jones CG, Sellar A, Storkey D, Blockley E, Stringer M et al (2018) The low-resolution version of HadGEM3 GC3.1: Development and evaluation for global climate. J Adv Model Earth Syst 10:2865–2888. https://doi.org/10.1029/2018MS001370
Lai WKM, Robson JI, Wilcox LJ, Dunstone N (2022) Mechanisms of internal atlantic multidecadal variability in HadGEM3-GC3.1 at two different resolutions. J Clim 35:1365–1383. https://doi.org/10.1175/JCLI-D-21-0281.1
Leapple T, Huybers P (2013) Reconciling discrepancies between Uk37 and Mg/Ca reconstructions of Holocene marine temperature variability. Earth Planet Sci Lett 375:418–429. https://doi.org/10.1016/j.epsl.2013.06.006
Lique C, Thomas MD (2018) Latitudinal shift of the Atlantic meridional overturning circulation source regions under a warming climate. Nat Clim Change 8:1013–1020. https://doi.org/10.1038/s41558-018-0316-5
Liu W, Fedorov AV, Xie S-P, Hu S (2020) Climate impacts of a weakened Atlantic meridional overturning circulation in a warming climate. Sci Adv 6:eaaz4876. https://doi.org/10.1126/sciadv.aaz4876
Ma L, Jiang Z (2023) Impacts of the strengthened Atlantic meridional overturning circulation on the North Atlantic sea surface temperature: mean state. Clim Dyn 61:981–998. https://doi.org/10.1007/s00382-022-06605-6
Marshall J, Scott JR, Romanou A, Kelley M, Leboissetier A (2017) The dependence of the ocean's MOC on mesoscale eddy diffusivities: a model study. Ocean Model 111:1–8. https://doi.org/10.1016/j.ocemod.2017.01.001
Meccia VL, Fuentes-Franco R, Davini P et al (2023) Internal multicentennial variability of the Atlantic Meridional Overturning Circulation simulated by EC-Earth3. Clim Dyn 60:3695–3712. https://doi.org/10.1007/s00382-022-06534-4
Megann A, Blaker A, Josey S, New A, Sinha B (2021) Mechanisms for late 20th and early 21st century decadal AMOC variability. J Geophys Res Oceans 126:e2021JC017865. https://doi.org/10.1029/2021JC017865
Menary MB et al (2020a) Aerosol-forced AMOC changes in CMIP6 historical simulations. Geophys Res Lett. https://doi.org/10.1029/2020GL088166
Menary MB, Jackson LC, Lozier MS (2020b) Reconciling the relationship between the AMOC and Labrador Sea in OSNAP observations and climate models. Geophys Res Lett 47:e2020GL089793. https://doi.org/10.1029/2020GL089793
Pausata FSR, Chafik L, Caballero R, Battisti DS (2015) Impacts of high-latitude volcanic eruptions on ENSO and AMOC. Proc Natl Acad Sci 112:13784–13788. https://doi.org/10.1073/pnas.1509153112
Petit T, Lozier MS, Josey SA, Cunningham SA (2021) Role of air–sea fluxes and ocean surface density in the production of deep waters in the eastern subpolar gyre of the North Atlantic. Ocean Sci 17:1353–1365. https://doi.org/10.5194/os-17-1353-2021
Rayner NA, Parker DE, Horton EB, Folland CK, Alexander LV, Rowell DP, Kent EC, Kaplan A (2003) Global analyses of sea surface temperature, sea ice, and night marine air temperature since the late nineteenth century. J Geophys Res Atmos. https://doi.org/10.1029/2002JD002670
Reintges A, Martin T, Latif M, Keenlyside NS (2017) Uncertainty in twenty-first century projections of the Atlantic Meridional Overturning Circulation in CMIP3 and CMIP5 models. Clim Dyn 49:1495–1511. https://doi.org/10.1007/s00382-016-3180-x
Roberts CD, Palmer MD (2012) Detectability of changes to the Atlantic meridional overturning circulation in the hadley centre climate models. Clim Dyn 39:2533–2546. https://doi.org/10.1007/s00382-012-1306-3
Roberts CD, Jackson L, McNeall D (2014) Is the 2004–2012 reduction of the Atlantic meridional overturning circulation significant? Geophys Res Lett 41:3204–3210. https://doi.org/10.1002/2014GL059473
Robson J, Ortega P, Sutton R (2016) A reversal of climatic trends in the North Atlantic since 2005. Nature Geosci 9:513–517. https://doi.org/10.1038/ngeo2727
Sellar AA et al (2020) Implementation of UK earth system models for CMIP6. J Adv Model Earth Syst 12:e2019MS00946. https://doi.org/10.1029/2019MS001946
Sellar AA et al (2019) UKESM1: description and evaluation of the UK earth system model. J Adv Model Earth Syst 11:4513–4558. https://doi.org/10.1029/2019MS001739
Srokosz M, Danabasoglu G, Patterson M (2021) Atlantic Meridional overturning circulation: reviews of observational and modeling advances—an introduction. J Geophys Res Oceans 126:e2020JC016745. https://doi.org/10.1029/2020JC016745
Voldoire A et al (2019) Evaluation of CMIP6 DECK experiments With CNRM-CM6-1. J Adv Model Earth Syst 11:2177–2213. https://doi.org/10.1029/2019MS001683
Weijer W, Cheng W, Garuba OA, Hu A, Nadiga BT (2020) CMIP6 models predict significant 21st century decline of the Atlantic meridional overturning circulation. Geophys Res Lett. https://doi.org/10.1029/2019GL086075
Xu X, Chassignet EP, Wang F (2019) On the variability of the Atlantic meridional overturning circulation transports in coupled CMIP5 simulations. Clim Dyn 52:6511–6531. https://doi.org/10.1007/s00382-018-4529-0
Yan X, Zhang R, Knutson TR (2018) Underestimated AMOC variability and implications for AMV and predictability in CMIP models. Geophys Res Lett 45:4319–4328. https://doi.org/10.1029/2018GL077378
Ye A, Zhu Z, Zhang R, Xiao Z, Zhou L (2023) Influence of solar forcing on multidecadal variability in the Atlantic meridional overturning circulation (AMOC). Front Earth Sci. https://doi.org/10.3389/feart.2023.1165386
Yeager SG, Robson JI (2017) Recent progress in understanding and predicting atlantic decadal climate variability. Curr Clim Change Rep 3:112–127. https://doi.org/10.1007/s40641-017-0064-z
Yeager S et al (2021) An outsized role for the Labrador Sea in the multidecadal variability of the Atlantic overturning circulation. Sci Adv 7:eabh3592. https://doi.org/10.1126/sciadv.abh3592
Zhang R, Thomas M (2021) Horizontal circulation across density surfaces contributes substantially to the long-term mean northern Atlantic Meridional Overturning Circulation. Commun Earth Environ 2:1–12. https://doi.org/10.1038/s43247-021-00182-y
Zhang RS, Danabasoglu G, Kwon Y, Marsh R, Yeager SG, Amrhein DE, Little CM (2019) A review of the role of the Atlantic Meridional Overturning Circulation in Atlantic multidecadal variability and associated climate impacts. Rev Geophys 57:316–375. https://doi.org/10.1029/2019RG000644